Supporting Information

Triplet Conformation in Chromophore-fused Cyclooctatetraene Dyes

Sunandita Paul,[a] Hidetsugu Kitakado,[b] Kensuke Suga,[b] Ryota Kotani,[b] Nilanjan Dey[b], Ravindra Venkatramani,[a] Eduard Matito[c], Shohei Saito[2]* and Jyotishman Dasgupta[a]*

1. Department of Chemical Sciences, Tata Institute of Fundamental Research, Mumbai, India
2. Department of Chemistry, Graduate School of Science, Kyoto University, Kyoto, Japan
3. Donostia International Physics Center (DIPC), Manuel Lardizabal Ibilbidea 4, 20018 Donostia, Euskadi, Spain

*Email: saito.shohei.4c@kyoto-u.ac.jp and dasgupta@tifr.res.in

Contents:

Materials and Methods:

Chemicals Used: FLAP, N-FLAP, anthraceneimide wing, and phenazine wing were synthesized as per the reported protocols in the literature[1-2]. All other HPLC-grade solvents were purchased from Sigma Aldrich and used as received.

Steady State Optical Spectroscopy: Steady state absorption measurements were carried out with JASCO V-670 spectrophotometer. All steady state emission measurements were done in Flourolog-3 (Horiba Jobin Yvon Inc) spectrofluorometer with Xe lamp as excitation source and PMT detector.

For steady state absorption and emission measurements were done in 10 μM of FLAP and N-FLAP solution in DCM and DCE. It was prepared by diluting a 100 μM stock solution. Excitation spectra were recorded at 1 μM concentration to avoid inner filter effect.

Time resolved Emission measurements: Lifetime measurement for the emissive states were determined by Time correlated single photon counting (TCSPC). Florescence photons were detected at the magic angle 54.7° to avoid anisotropy effects by a microchannel plate photomultiplier (model R2809; Hamamatsu Corp.) which was coupled to a single photon counting setup. Excitation was done with a 400 nm picosecond laser pulse for FLAP and 295 nm for N-FLAP. The 400 nm was generated by frequency doubling a 800 nm output pulse from a modelocked Ti-sapphire laser (Tsunami, Spectra-Physics, USA) (720−900 nm) on being pumped by a diode CW Nd Vanadate laser (532nm) (Millennia X, Spectra-Physics, USA). Pulse width and repetition rate was 1−2 ps and 80 MHz respectively. Instrument response function was measured by scattering photons using a colloidal suspension of dried nondairy coffee whitener. All TCSPC measurements were done in 100 μM of FLAP and N-FLAP.

Femtosecond Transient Absorption Measurements: Time resolved absorption measurements were done using femtosecond transient absorption setup which has been described in details previously. Briefly, a mode-locked femtosecond (~10 fs) pulse was generated using Ti-Sapphire crystal with bandwidth of ~100 nm and ~400 mW power at a repetition rate of 80 MHz (Coherent Micra-5 Mode-locked Ti:sapphire Laser system). It was then amplified using chirp pulse amplification in a commercial regenerative amplifier

(Coherent Legend Elite Ultrafast Amplifier Laser system) to produce ~30 fs pulses at 800 nm (65 nm bandwidth) with 3.5 mW power and 1 KHz repetition rate. Generation of 400 nm pump pulse was done by frequency doubling a portion of the 800 nm pulse generated from the amplifier by a 2 mm BBO crystal. The power of the pump pulse was kept at 200 nJ at sample stage for all measurements. A white light continuum was generated by focusing a small portion of the 800 nm pulse from the amplifier on a sapphire crystal. This was used as a probe which was ~15 fs (420 nm - 1400 nm) in width. The pump was passed through a onemeter-long motorized delay stage for setting the time difference between the pump and probe. Both the pump and the probe were focused on the sample stage spatially and temporally. All measurements were carried out in a 2 mm flow cuvette connected to a peristaltic pump to circulate the liquid for avoiding any sample photodegradation. The IRF was ~200 fs for the measurements. All measurements were done in inert condition under Argon atmosphere at 100μM concentration and 200nJ power per pulse.

Nanosecond Transient Absorption Measurements: Pump-probe measurements with nanosecond to micro-second time delays were carried out using a commercially available Ultrafast Systems EOS set up as described earlier[3].The pump beam was generated by the commercial OPA pumped by the Legend Elite amplifier (described above) routed to the sample. The white light supercontinuum was generated by photonic crystal fibre waveguides which was being pumped by sub nanosecond Nd:YAG laser. The continuum has a spectral

bandwidth from ~380-1600 nm with a 2 kHz repetition rate. The time delay is electronically controlled which ranges from 1 ns to 400 µs. The pump and the probe were again spatially and temporally overlapped on the same 2 mm flow cuvette. The IRF was ~100 ps for all measurements.

Kinetic Data Fitting Procedure: Single wavelength kinetic fits for transient absorption and TCSPC was fitted using multi exponential decay constants in convolution with the respective IRFs. It was done in Igor Pro wavematrics software to get the lifetime and amplitude of each decay component. The equation used was: $y = A_0 + \sum_1^n a_i \, e^{-t/T_i}$

Global Analysis of TA data: Global analysis of the TA data was done using Glotaran 1.5.1 software. Single value decomposition was done to obtain the species associated spectra (SADS) and their corresponding lifetimes[4].

Computational Details: All calculations were done using Gaussian 16.[5] The ground state geometries of **FLAP** and **N-FLAP** were optimized using the DFT method with PBE0 functional and 6-31G(d) basis set. The excited state optimizations of FLAP at the S_2 bent, S_1 bent and S_1 planar geometries were performed at the TD-PBE0/6-31G(d) level. Triplet geometries were optimized at the UPBE0/6-31G(d) level. All geometries showed true minima with no imaginary vibrational mode. TD-DFT calculations were performed to simulate the triplet-triplet transitions. Calculations for simplified chemical structures (**FLAP′** and **N-FLAP′**) were performed at the UPBE0/6-31+G(d) level. In constrained geometry optimization at the triplet ground state, ModRedundant keyword was used to fix bent angles. Standard aromaticity indices of the nucleus-independent chemical shifts (NICS),[6] the harmonic oscillator model of aromaticity (HOMA),[7a] HOMA for heterocycle electron delocalization (HOMHED),[7b] the anisotropy of the current induced density (ACID),[8] and the electron-sharing criteria such as the aromatic fluctuation index (FLU)[9] and the multicenter

index (MCI)[10] were computed for the optimized geometries at the local minimum in T_1 with planar C_{2v} symmetry. NICS values at the center of the benzene, pyrazine, and COT rings were calculated with the gauge-independent atomic orbital (GIAO) method. HOMA and HOMHED values were calculated along the local rings and the peripheral macrocycles. ACID calculations were performed with the continuous set of gauge transformations (CSGT) method. In the constrained geometry optimization and aromaticity calculations, terminal functional groups were replaced by hydrogen atoms for **FLAP** (**FLAP′**) and methyl groups for **N-FLAP** (**N-FLAP′**) to reduce calculation cost. FLU and MCI calculations were performed with AIMAll (Version 19.10.12) [11] and ESI-3D[12] programs.
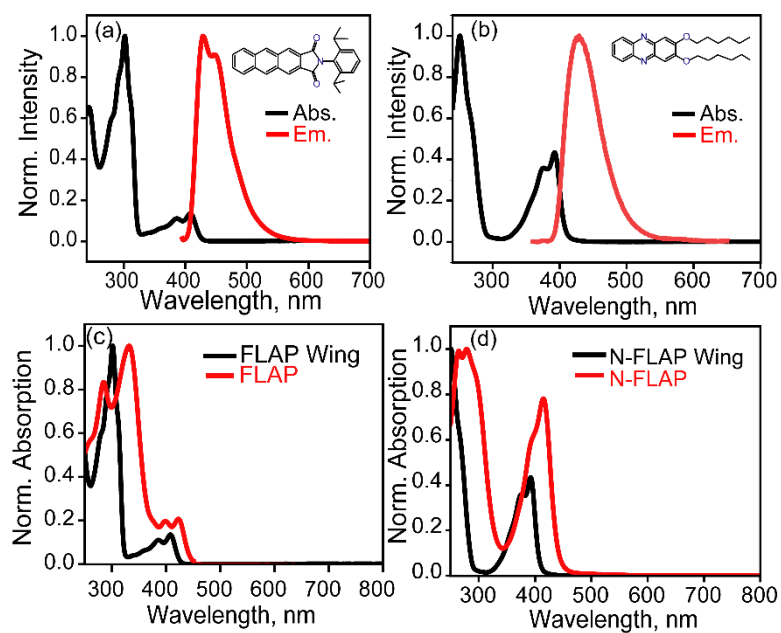
Figure S1. (a) Absorption (black trace) and emission (red trace) spectra for (b) anthraceneimide wing in DCM (b) phenazine wing in DCM. (c) Comparison of absorption spectra of FLAP and its anthraceneimide wing in DCM. (d) Comparison of absorption spectra of N-FLAP and its phenazine wing in DCM.
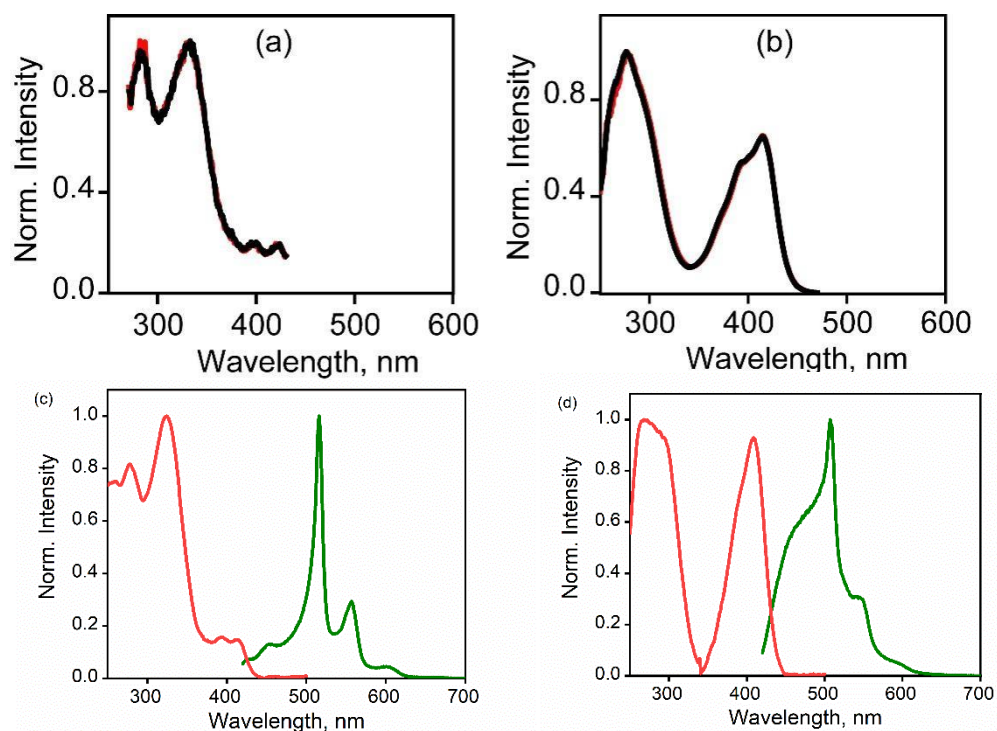
Figure S2. Fluorescence excitation spectra of (a) FLAP and (b) N-FLAP in DCM (black) and DCE (red) respectively. (c) Absorption and emission spectra of FLAP in mineral oil (d)) Absorption and emission spectra of N-FLAP in mineral oil.
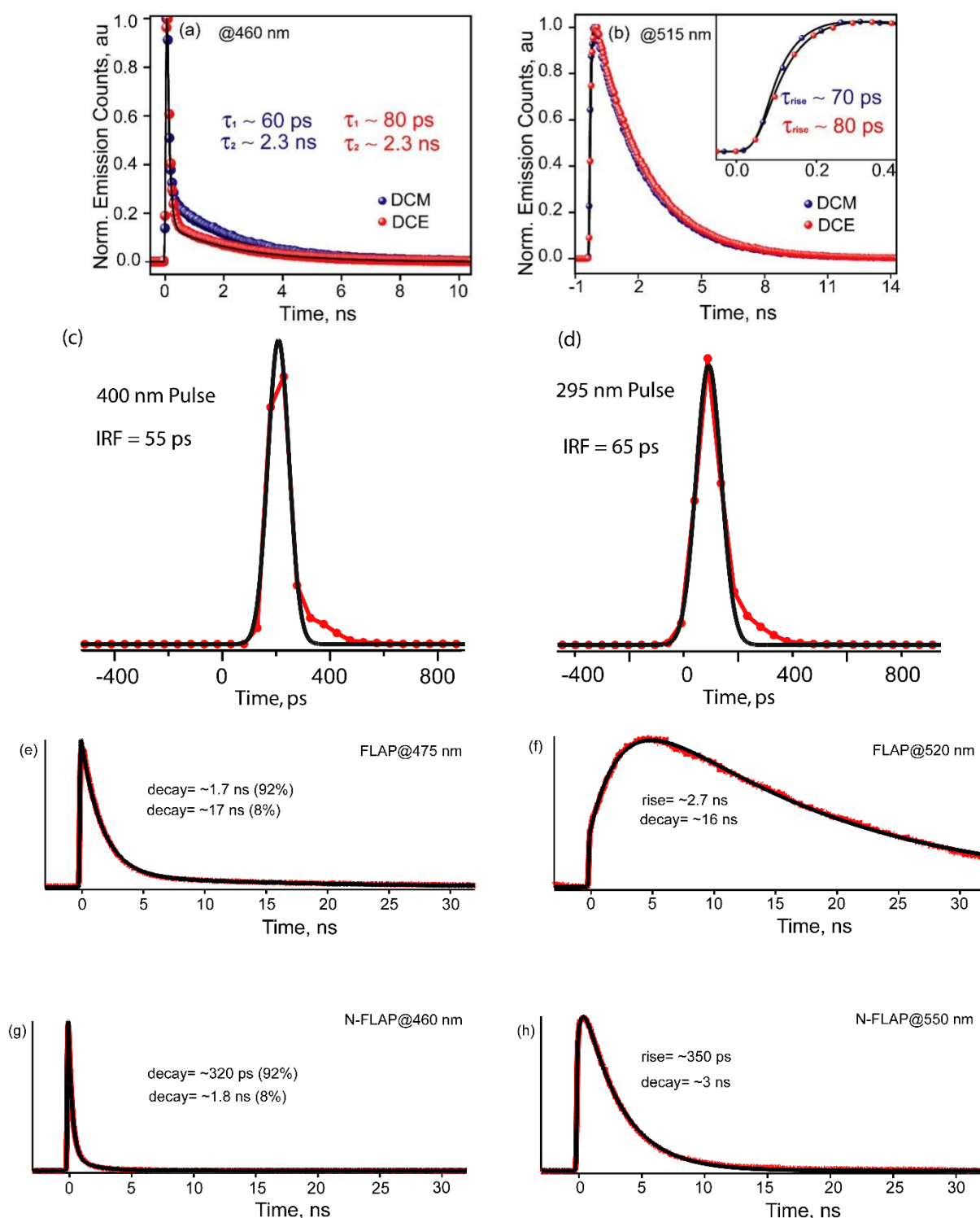
Figure S3. Time-correlated single photon counting measurements: Emission lifetime of N-FLAP in DCM (blue trace) and DCE (red trace) subsequent to 295 nm excitation monitored at (a) 460 nm (b) 515 nm. IRF of both the TCSPC set up with 400 nm excitation (used for FLAP) and 295 nm excitation (used for N-FLAP are shown for (c) 400 nm pulse (d) 295 nm pulse. Emission lifetime of FLAP in mineral oil subsequent to 295 nm excitation monitored at (e) 475 nm (f) 520 nm. Emission lifetime of N-FLAP in mineral oil subsequent to 295 nm excitation monitored at (g) 460 nm (h) 550 nm
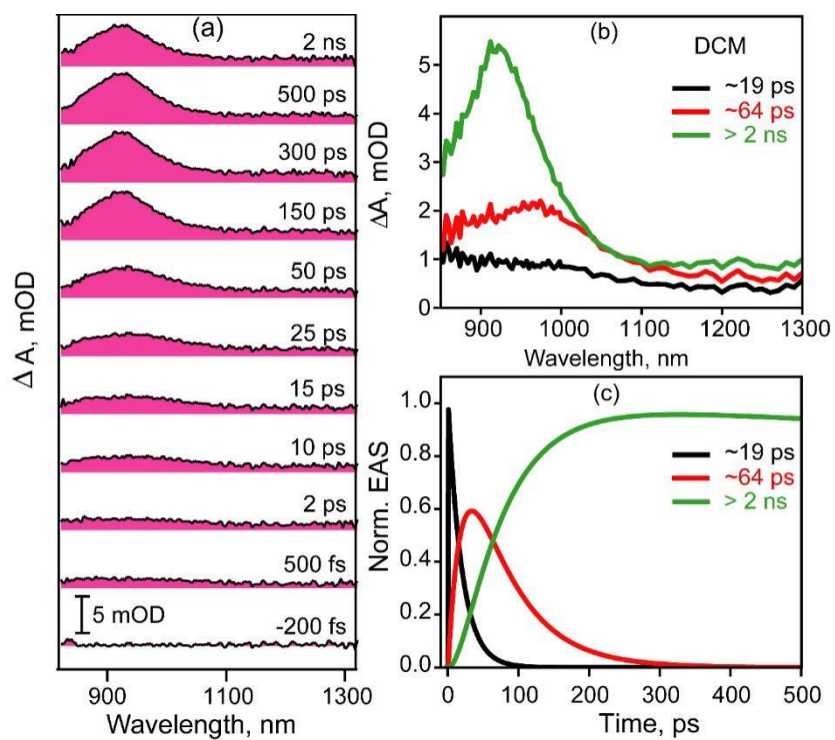
Figure S4. (a) Femtosecond transient absorption spectra at various time delays for FLAP in DCM. The spectral traces are shown in the NIR range in between 850 nm to 1300 nm. (b) SVD showing the evolution associated spectra (EAS) for a three-state sequential model with the corresponding lifetimes. (c) The fitted kinetics after SVD for the three-state sequential model.
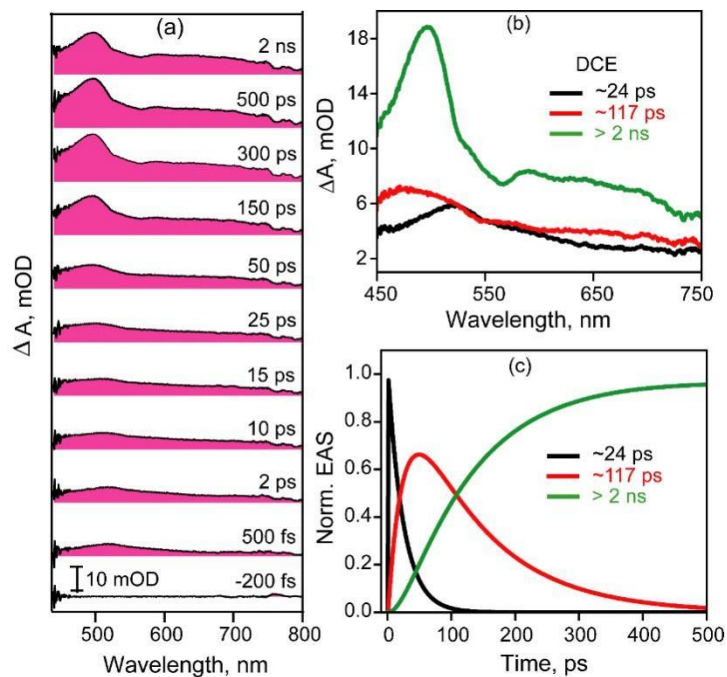
Figure S5. (a) Femtosecond transient absorption spectra at various time delays for FLAP in DCE. The spectral traces are shown in the visible range i.e. from 440 nm to 750 nm. (b) SVD showing the evolution associated spectra (EAS) for a three-state sequential model with the corresponding lifetimes. (c) The fitted kinetics after SVD for the three-state sequential model.
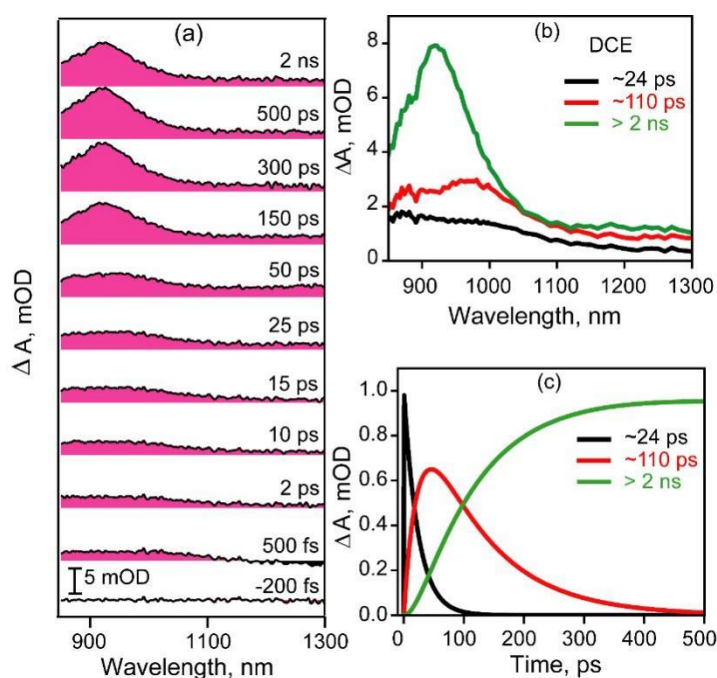
Figure S6. (a) Femtosecond transient absorption spectra at various time delays for FLAP in DCE. The spectral traces are shown in the NIR range in between 850 nm to 1300 nm. (b) SVD showing the EAS for a three-state sequential model with the corresponding lifetimes. (c) The fitted kinetics after SVD for the three-state sequential model.

Figure S7. (a) Femtosecond transient absorption spectra at various time delays for N-FLAP in DCM. The spectral traces are shown in the NIR range in between 850 nm to 1300 nm. (b) SVD showing the EAS for a three-state sequential model with the corresponding lifetimes. (c) The fitted kinetics after SVD for the three-state sequential model.

Figure S8. (a) Femtosecond transient absorption spectra at various time delays for N-FLAP in DCE. The spectral traces are shown in the visible range i.e. from 440 nm to 750 nm. (b) SVD showing the EAS for a three-state sequential model with the corresponding lifetimes. (c) The fitted kinetics after SVD for the three-state sequential model.
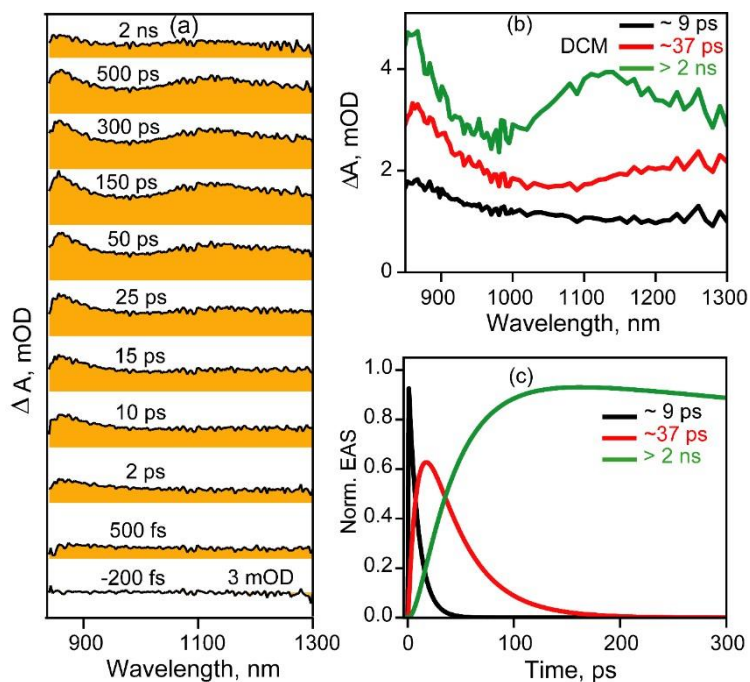
Figure S9. (a) Femtosecond transient absorption spectra at various time delays for N-FLAP in DCE. The spectral traces are shown in the NIR range in between 850 nm to 1300 nm. (b) SVD showing the EAS for a three-state sequential model with the corresponding lifetimes. (c) The fitted kinetics after SVD for the three-state sequential model.

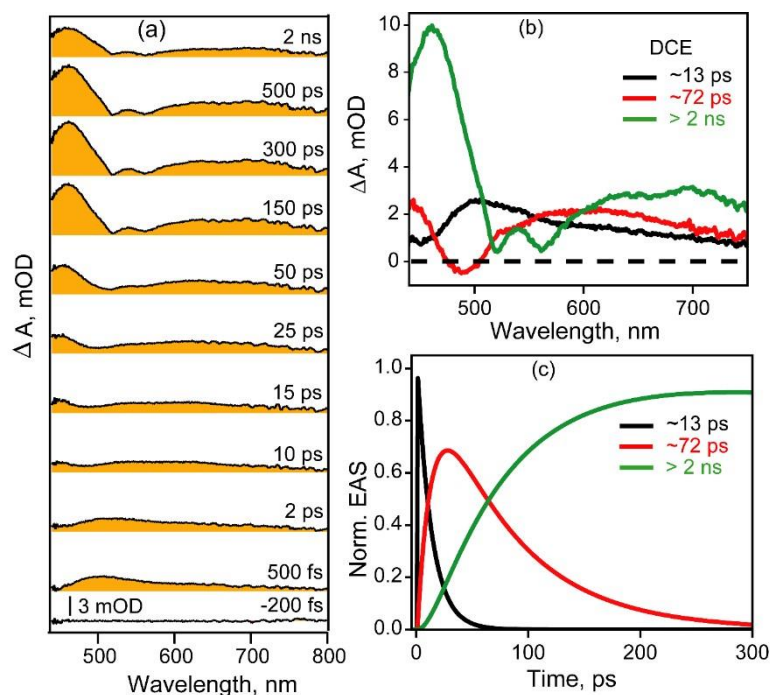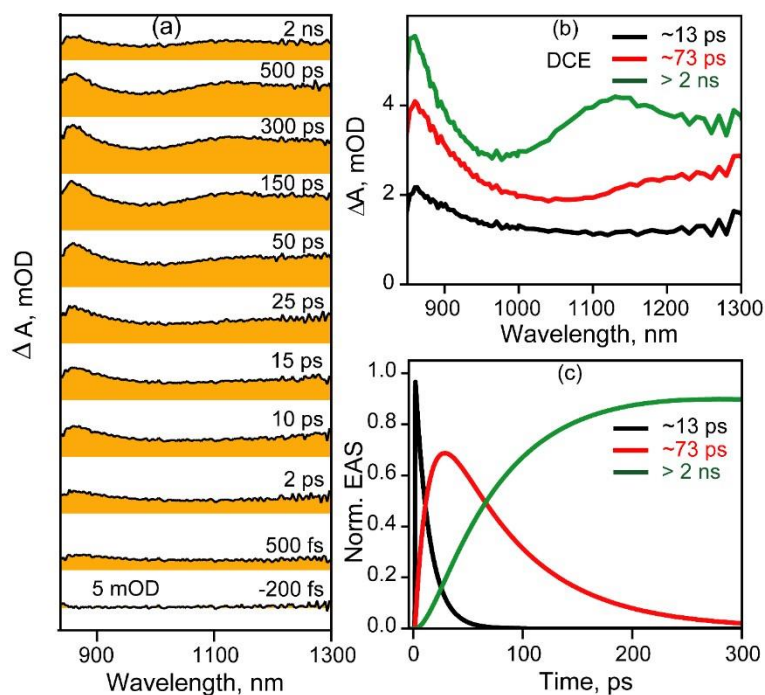

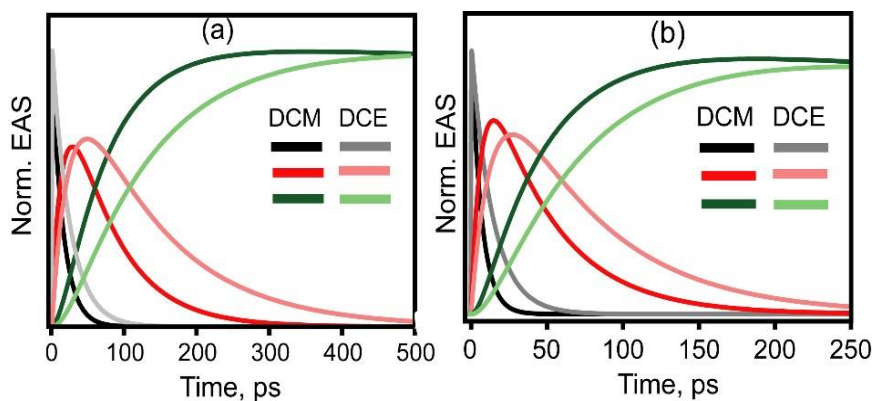**Figure S10.** (a) The fitted kinetics after SVD for the three-state sequential model in both DCM and DCE for FLAP in visible region from fs-ns. (b) The fitted kinetics after SVD for the three-state sequential model in both DCM and DCE for N-FLAP in visible region from fs-ns.
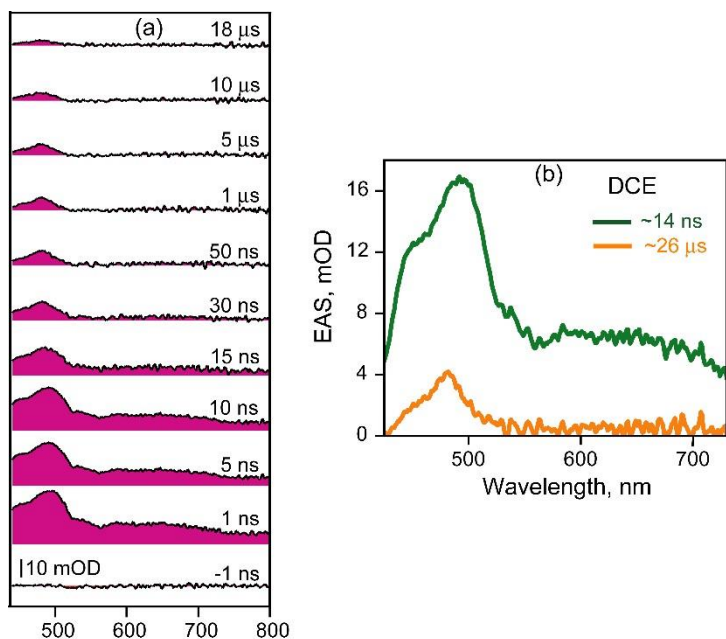
Figure S11. (a) Nanosecond-to-microsecond transient absorption spectra in the visible range at various time delays from 1 nanosecond to 18 microseconds for FLAP in DCE. (b) SVD of the entire spectrum into a two-state sequential model showing the corresponding spectra and lifetime
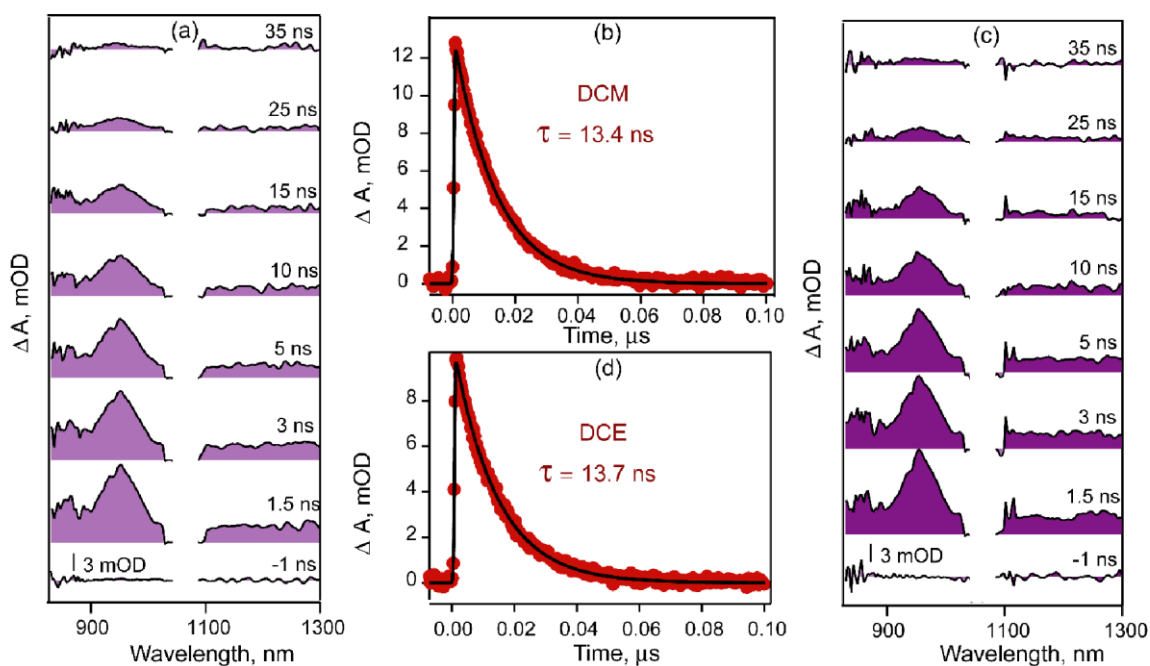
Figure S12. Nanosecond-to-microsecond transient absorption spectra in the NIR range at various time delays from 1 nanosecond to 35 nanoseconds for FLAP in (a) DCM and (c) in DCE. Single point kinetic fits showing a mono exponential decay at 952nm in (b) DCM and (d) DCE respectively.
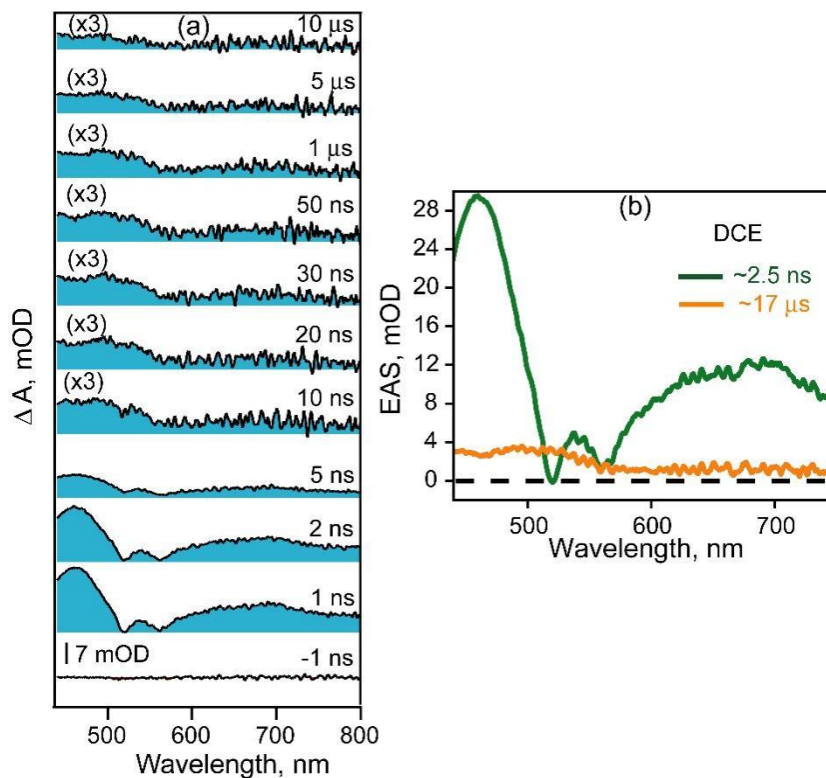
Figure S13. (a) Nanosecond-to-microsecond transient absorption spectra in the visible range at various time delays from 1 nanosecond to 10 microseconds for N-FLAP in DCE. (b) SVD of the entire spectrum into a two-state sequential model showing the corresponding spectra and lifetime.

Figure S14. Oxygen dependent triplet state quenching of N-FLAP in DCM. The kinetics is plotted at 457 nm subsequent to photoexcitation at 400 nm. A clear dependence of the triplet lifetime on the presence of O_2 provides support to the triplet assignment.
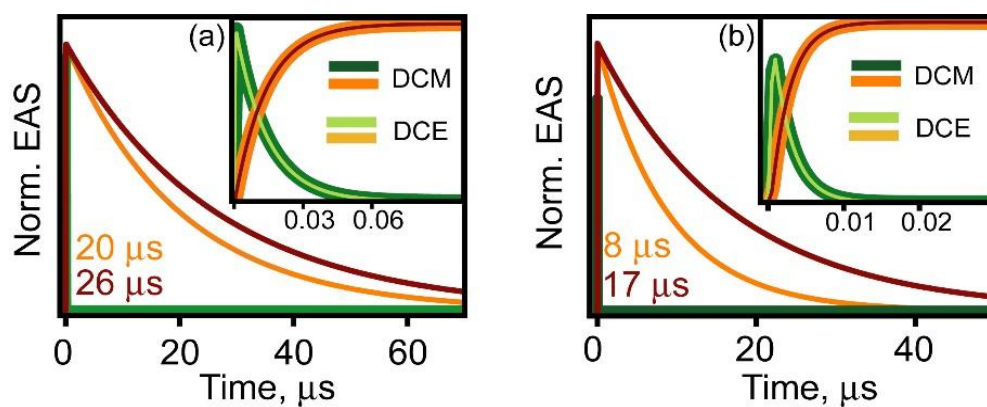
Figure S15. (a) The fitted kinetics after SVD for the two-state sequential model in both DCM and DCE for FLAP in visible region from ns- µs. (b) The fitted kinetics after SVD for the two-state sequential model in both DCM and DCE for N-FLAP in visible region from ns- µs.
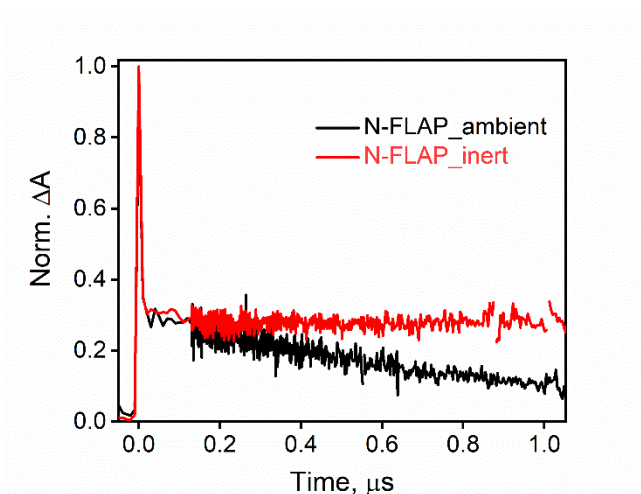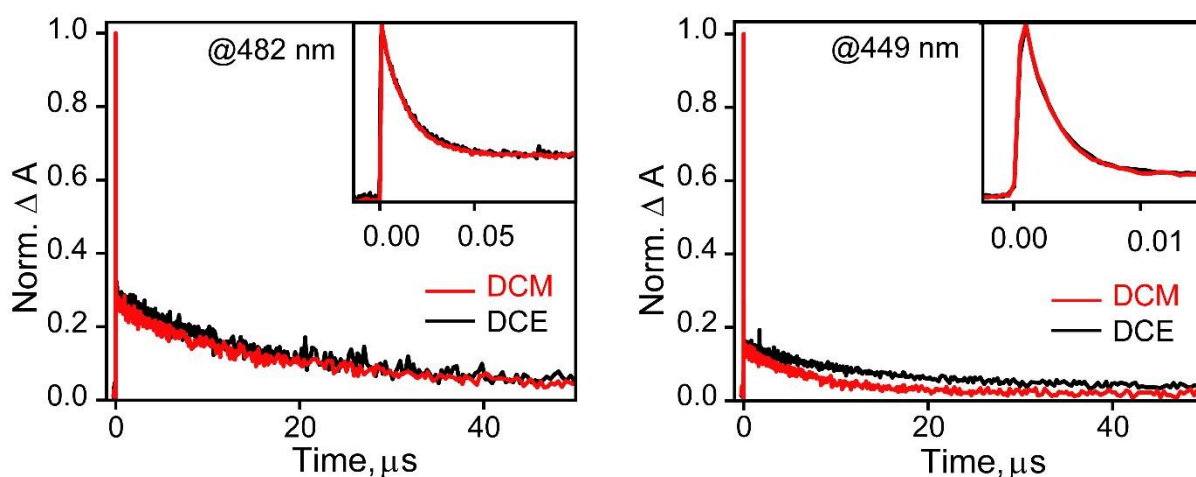

Figure S16. (a) Single point kinetics of FLAP showing viscosity dependent triplet lifetimes at 482 nm. (b) Single point kinetics of N-FLAP showing viscosity dependent triplet lifetimes at 449 nm.
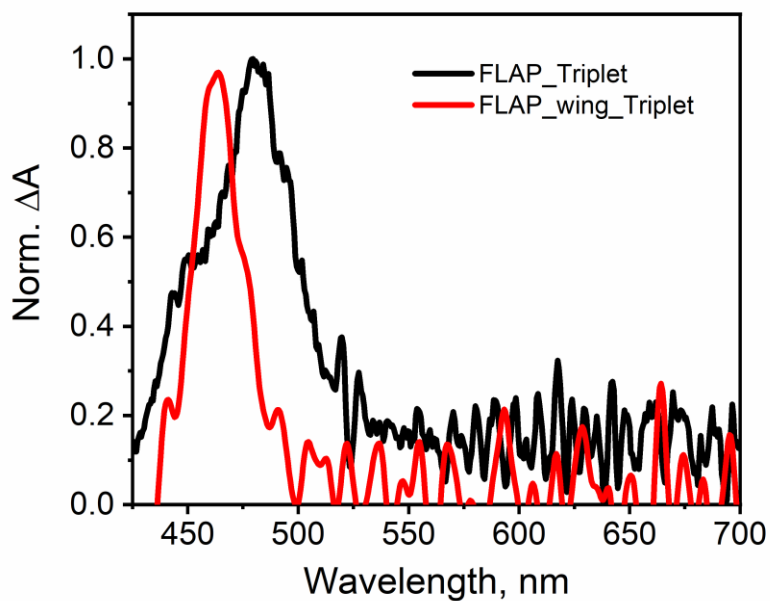
Figure S17. Comparison of triplet absorption spectra of anthraceneimide wing with full FLAP triplet absorption in DCM. Both the spectral traces are shown at 50 ns time delay.
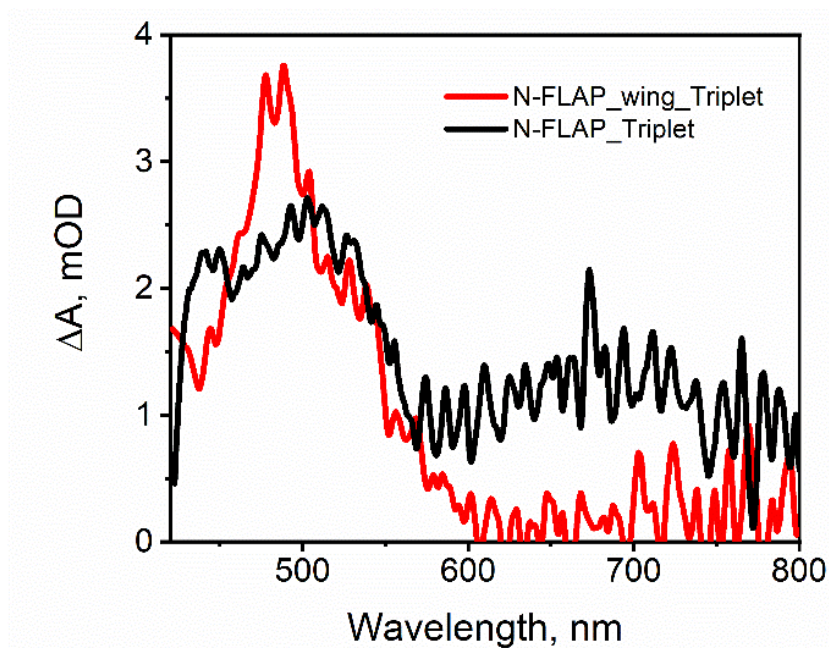
Figure S18. (a) Comparison of triplet absorption spectra of phenazine wing with full N-FLAP triplet absorption in DCM. Both the spectral traces are shown at 50 ns time delay..
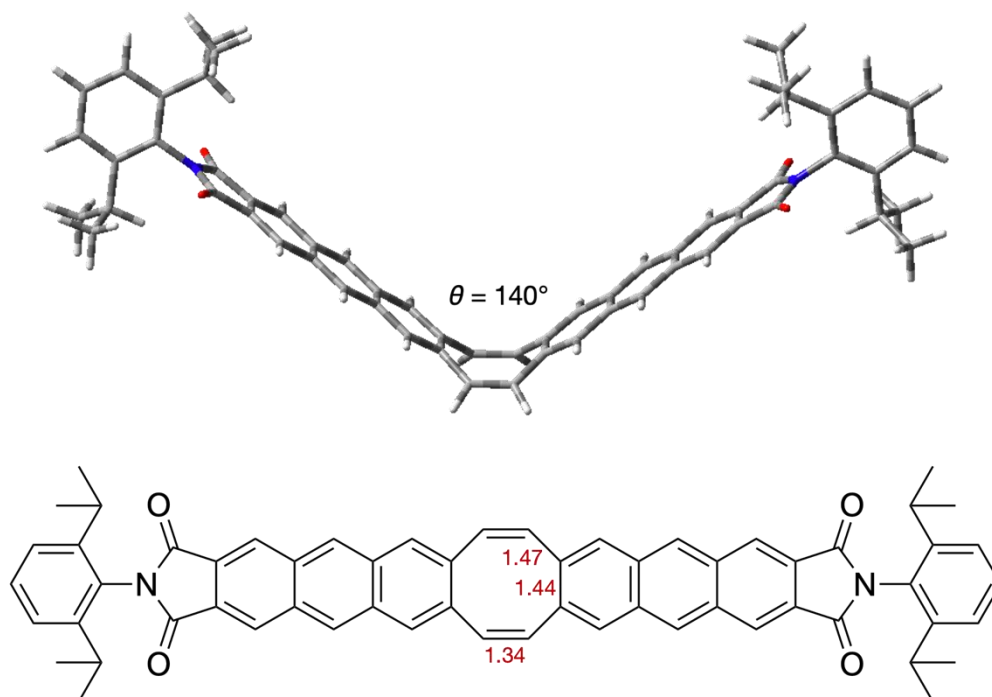
Figure S19. S_0 optimized geometry of FLAP at the PBE0/6-31G(d) level. The COT bent angle is 140°.

(a)

θ = 159°

1.38
1.43
1.44
1.46
1.35

(b)

θ = 180°

1.40
1.41
1.48
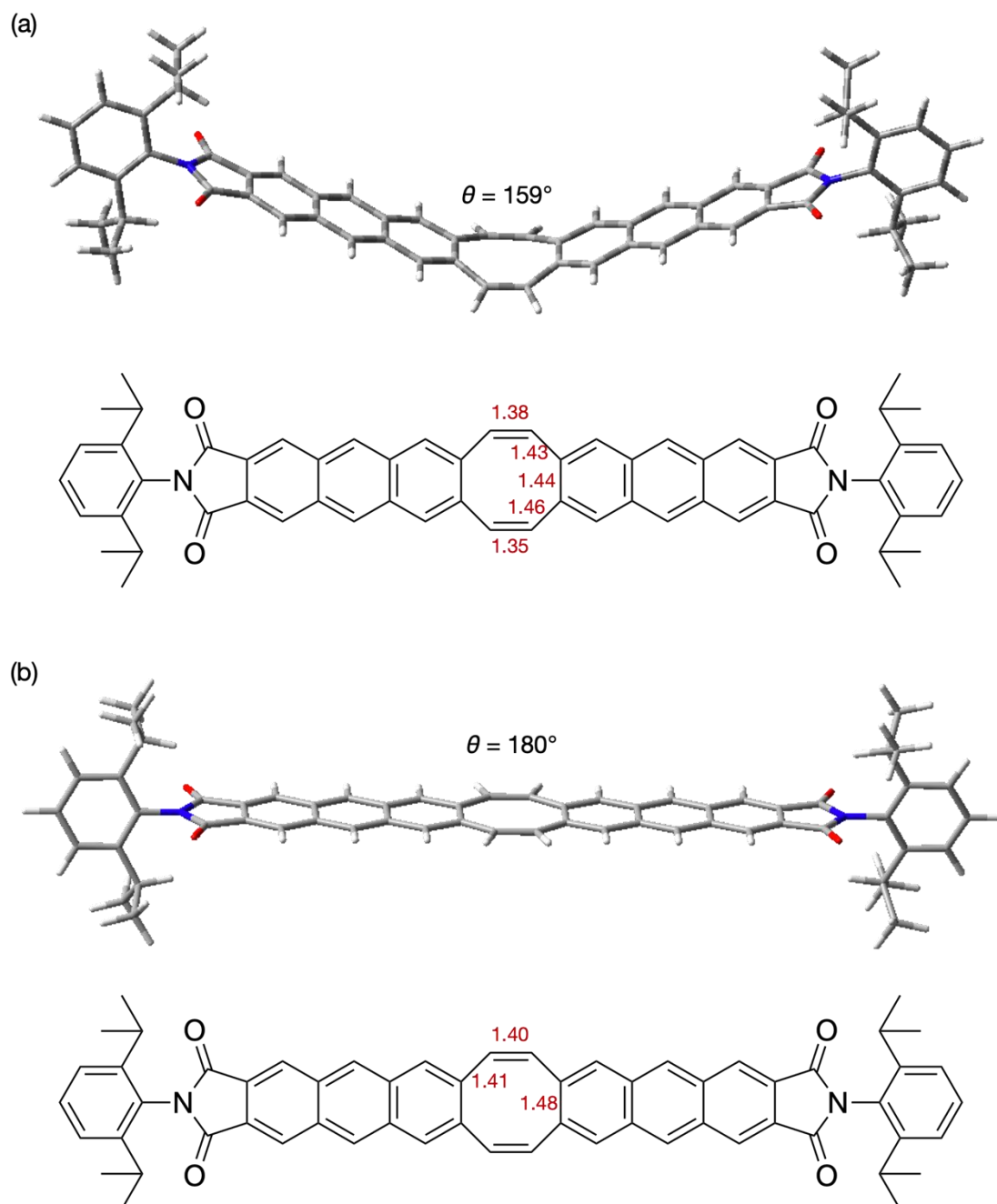
Figure S20. S$_1$ optimized geometries were obtained via vertical excitation to the S$_1$ surface. For the (a) V-shaped geometry energy optimization was performed after vertical excitation; and (b) planar FLAP geometry was obtained via vertical excitation from a planar transition state in the S$_0$ geometry at the TD-PBE0/6-31G(d) level. The COT bent angle is 159° and 180° respectively.
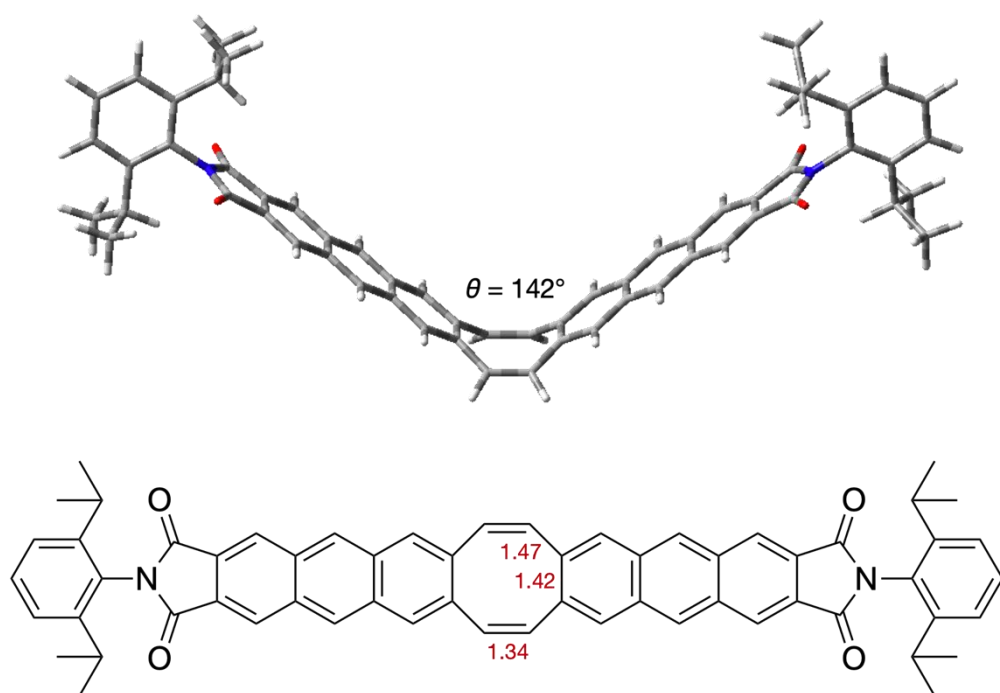
Figure S21. S_2 optimized geometry of FLAP obtained via a vertical excitation from the S_0 surface to the optically allowed S2 state along with optimization on the S_2 surface at the TD-PBE0/6-31G(d) level. The COT bent angle at the S_2 minima is 142°.
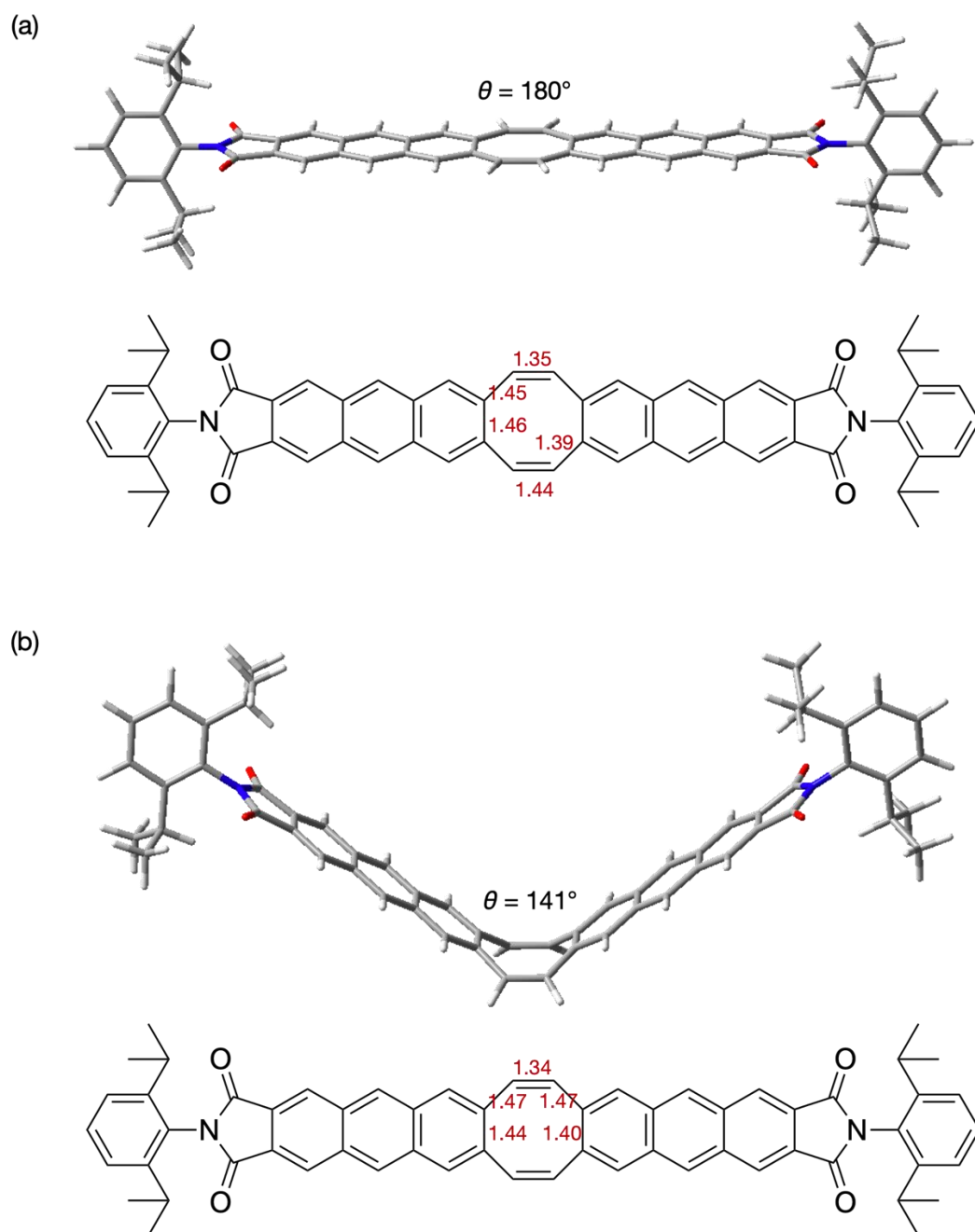
Figure S22. T_1 optimized geometries were obtained with a starting guess planar geometry while optimization on the triplet surface was initiated by defining the spin state to be S=1. We obtained the (a) planar triplet minima by optimization on the T1 surface while the (b) V-shaped FLAP was obtained by de-symmetrization of the COT bond-lengths on the T1 surface at the UPBE0/6-31G(d) level. The COT bent angle obtained were 180° and 141° respectively.
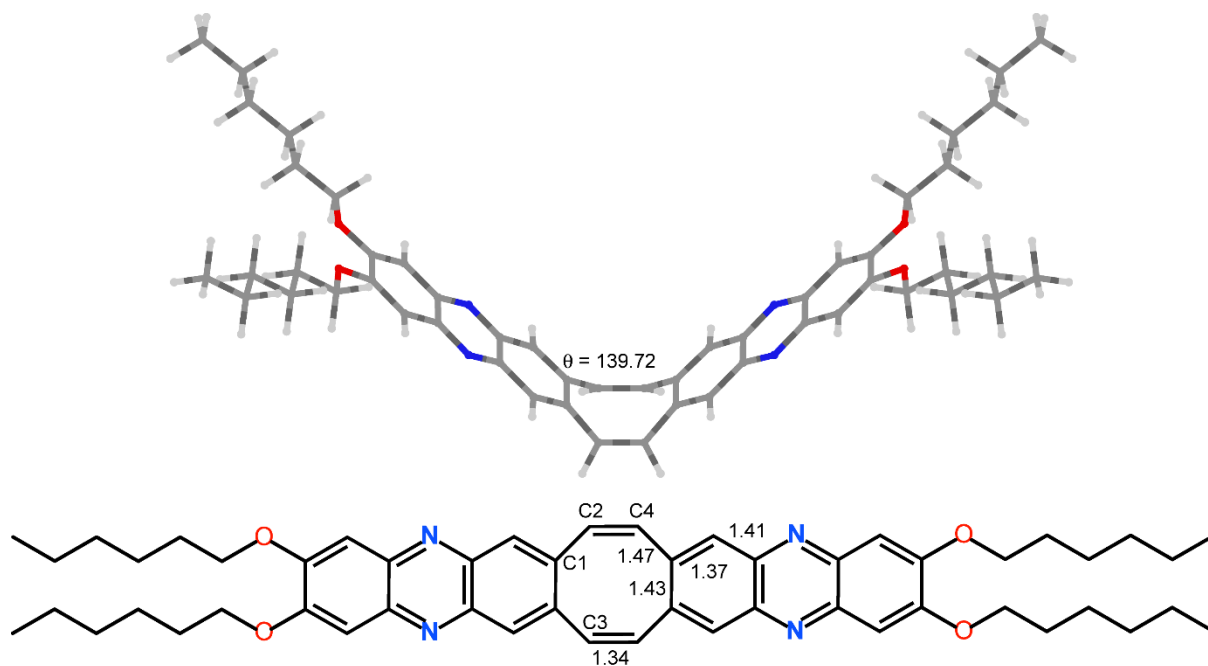
Figure S23. S_0 optimized geometry of N-FLAP at the PBE0/6-31G(d) level. The dihedral angle C1-C2-C3-C4 is 139.72°.
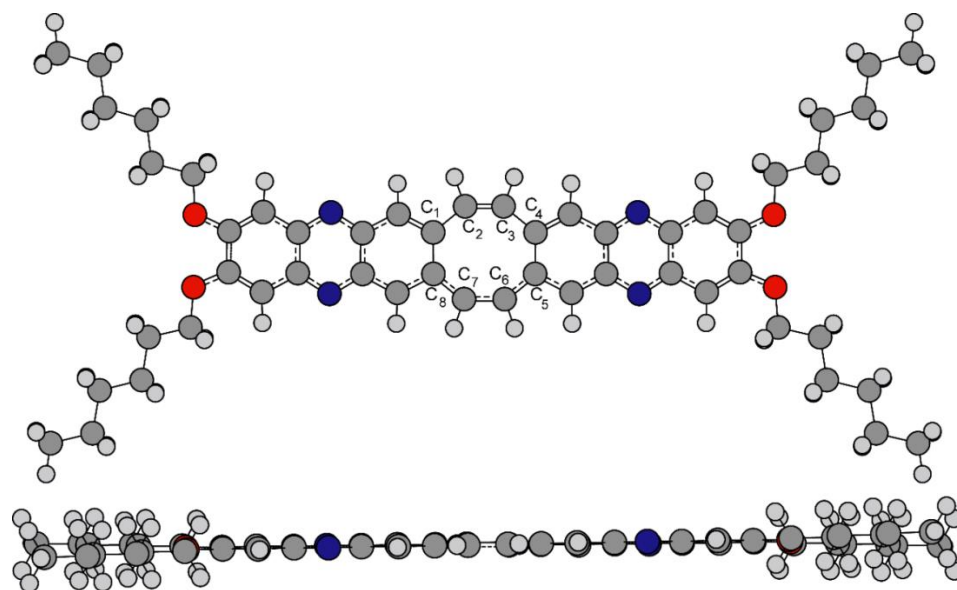
Figure S24. T_1 optimized geometry of N-FLAP (obtained as a local minimum) at the UPBE0/6-31G(d) level. The dihedral angle C1-C2-C7-C3 is 179.83°. The bond lengths (Å) are: C1-C2 1.45, C2-C3 1.35, C3-C4 1.45, C4-C5 1.46, C5-C6 1.38, C6-C7 1.44, C7-C8 1.38, C8-C1 1.44.
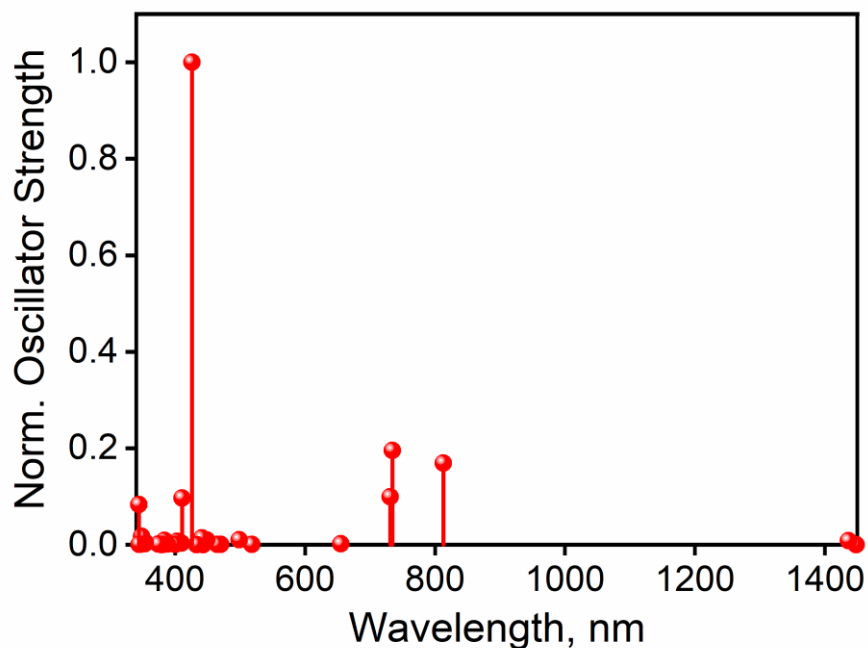
Figure S25. Computed TD-DFT transitions within the triplet manifold for full FLAP with planar geometry using UPBE0/6-31G(d). The stick spectrum in red indicates the transition probabilities to higher excited state with respect to specific energy values as shown in wavelength scale.
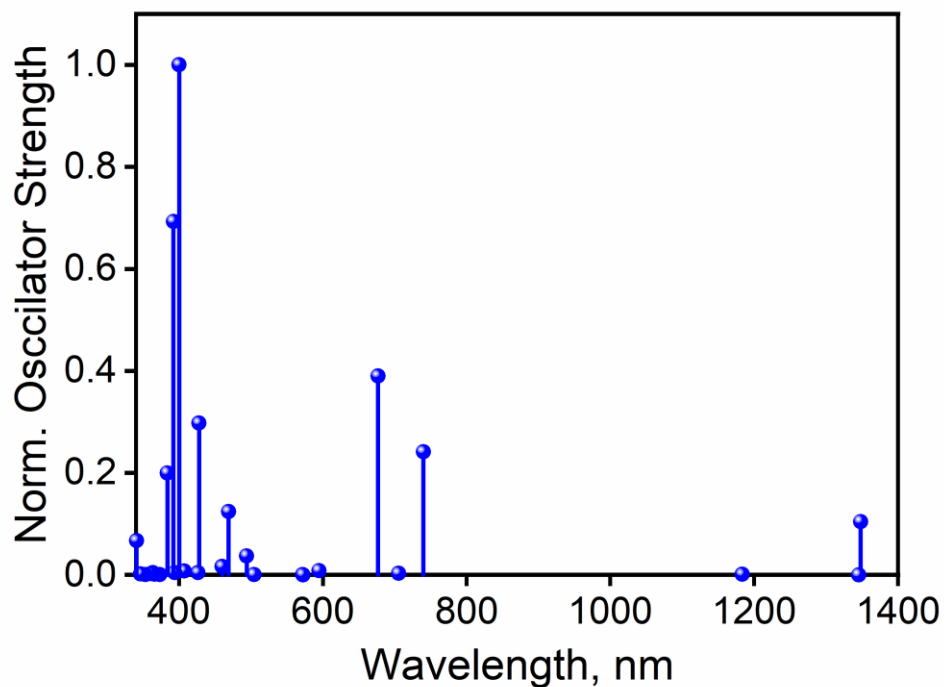
Figure S26. Computed TD-DFT transitions within the triplet manifold for full N-FLAP with planar geometry using UPBE0/6-31G(d). The stick spectrum in blue indicates the transition probabilities to higher excited state with respect to specific energy values as shown in wavelength scale.

Energy diagrams of optimized geometries in T_1

In constrained geometry optimization with fixed bent angles, the dihedral angle between C1-C2-C3 and C2-C3-C4 planes in Figure 9 was fixed using the ModRedundant keyword. Bent C_s geometries were obtained when started optimization from the initial geometries that have asymmetrical wings. In the optimization calculation, three geometries at the (local) minimums (planar C_{2v}, planar D_{2h} and bent C_s) were found. It was confirmed that these geometries do not have imaginary vibrations by frequency calculation.
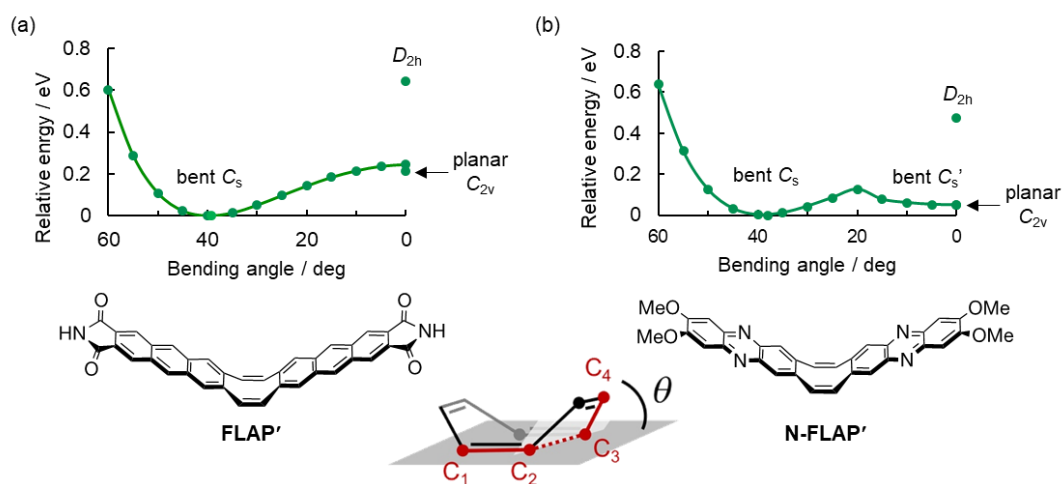
Figure S27. Energy profiles with respect to conformational planarization of (a) **FLAP′** and (b) **N-FLAP′** in the triplet ground state. The central inset figure shows the definition of the COT bending angle. Constrained structural optimizations were performed at the UPBE0/6-31+G(d) level of theory.

Optimized geometries in the T$_1$ state
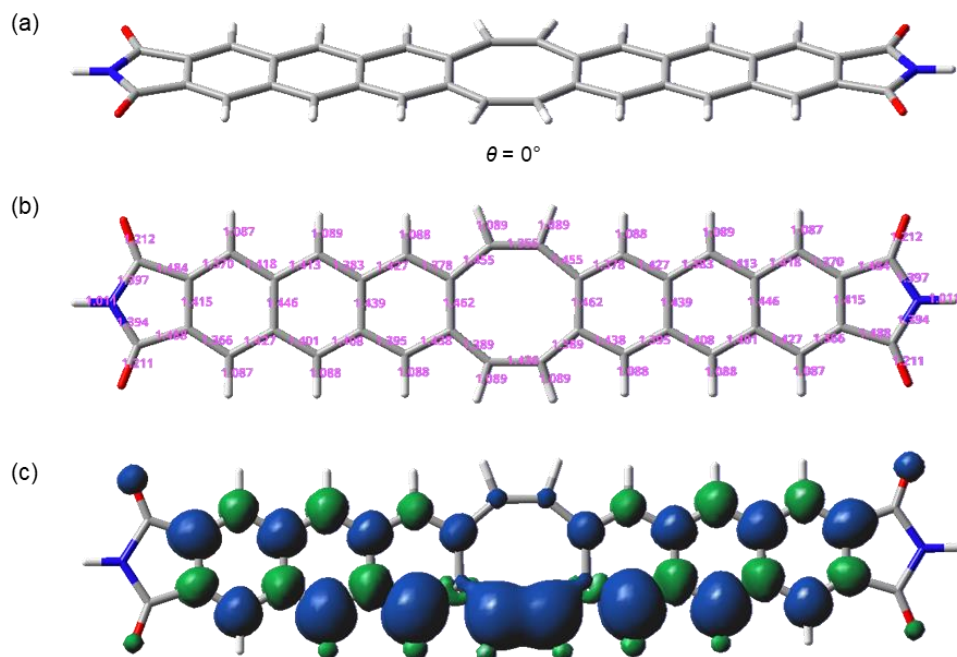
Figure S28. (a) The optimized geometry of **FLAP'** at the local minimum in T$_1$ with C_{2v} symmetry at the UPBE0/6-31+G(d) level of theory. (b) Bond length (Å) of **FLAP'**. (c) Spin-density-distribution plot of **FLAP'** in T$_1$ (isovalue: 0.0015).
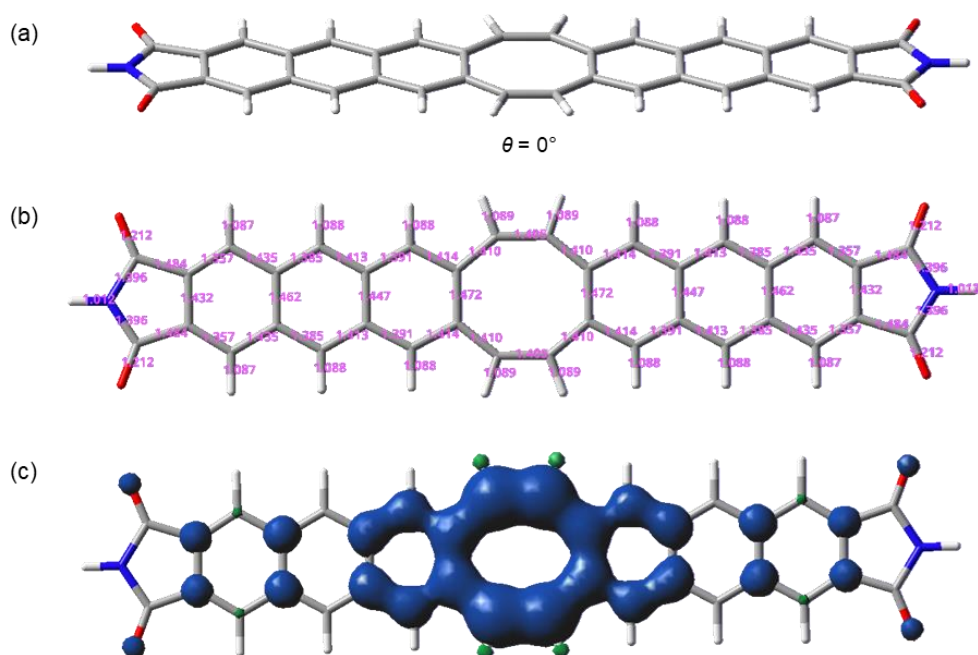
Figure S29. (a) The optimized geometry of **FLAP'** at the local minimum in T$_1$ with D_{2h} symmetry at the UPBE0/6-31+G(d) level of theory. (b) Bond length (Å) of **FLAP'**. (c) Spin-density-distribution plot of **FLAP'** in T$_1$ (isovalue: 0.0015).

(a)

$\theta = 39.2°, 40.4°$

(b)

(c)
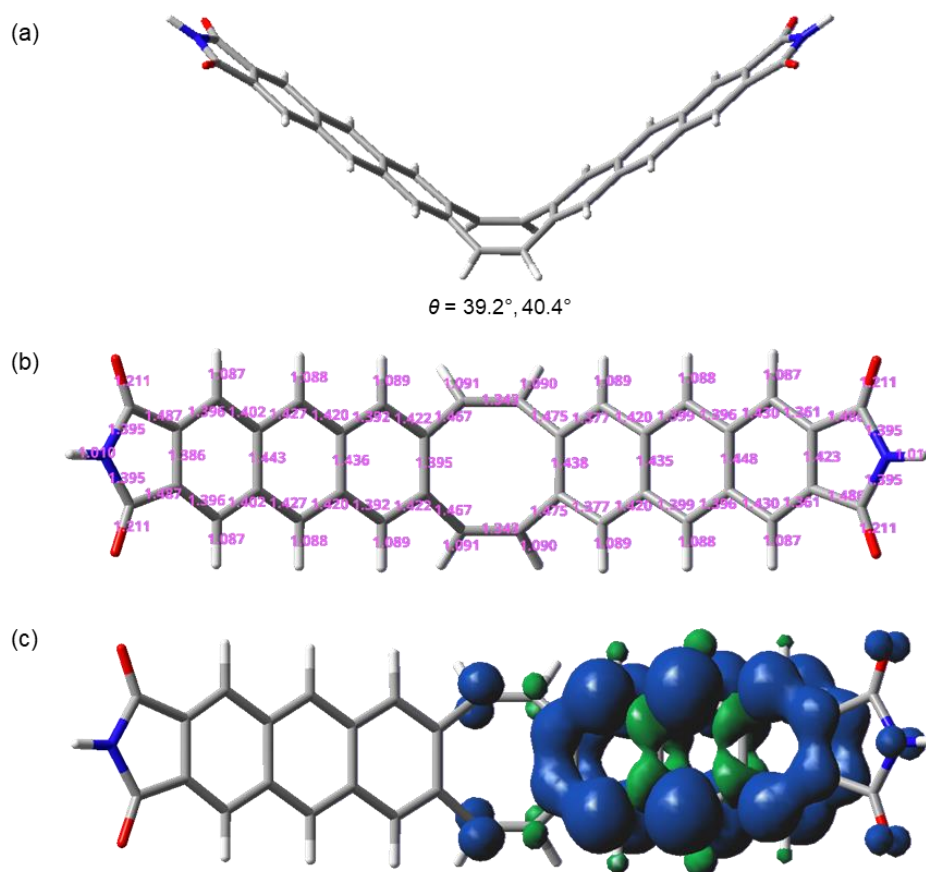
Figure S30. (a) The optimized geometry of **FLAP'** at the local minimum in T_1 with C_s symmetry at the UPBE0/6-31+G(d) level of theory. (b) Bond length (Å) of **FLAP'**. (c) Spin-density-distribution plot of **FLAP'** in T_1 (isovalue: 0.0015).

(a) UPBE0/6-31+G(d)

(b) UCAM-B3LYP/6-31+G(d)

(c) UωB97X/6-31+G(d)

Figure S31. Comparison of the total energy of **FLAP'** at the T_1 optimized geometries. The energy was calculated at the optimized geometries at the level of (a) UPBE0/6-31+G(d), (b) UCAM-B3LYP/6-31+G(d), and (c) UωB97X/6-31+G(d), respectively.

Figure S32. (a) The optimized geometry of **N-FLAP'** at the local minimum in T_1 with C_{2v} symmetry at the UPBE0/6-31+G(d) level of theory. (b) Bond length (Å) of **N-FLAP'**. (c) Spin-density-distribution plot of **N-FLAP'** in T_1 (isovalue: 0.0015).

Figure S33. (a) The optimized geometry of **N-FLAP'** at the local minimum in T_1 with D_{2h} symmetry at the UPBE0/6-31+G(d) level of theory. (b) Bond length (Å) of **N-FLAP'**. (c) Spin-density-distribution plot of **N-FLAP'** in T_1 (isovalue: 0.0015).
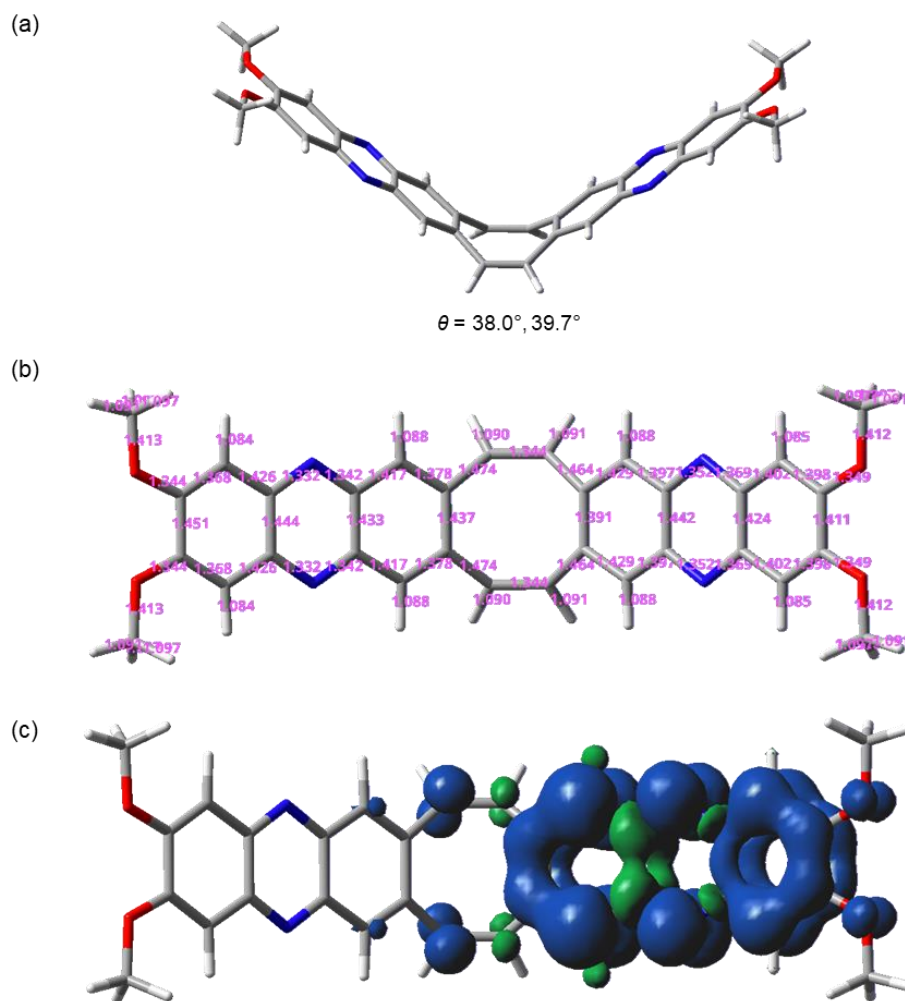
Figure S34. (a) The optimized geometry of **N-FLAP'** at the local minimum in T_1 with C_s symmetry at the UPBE0/6-31+G(d) level of theory. (b) Bond length (Å) of **N-FLAP'**. (c) Spin-density-distribution plot of **N-FLAP'** in T_1 (isovalue: 0.0015).
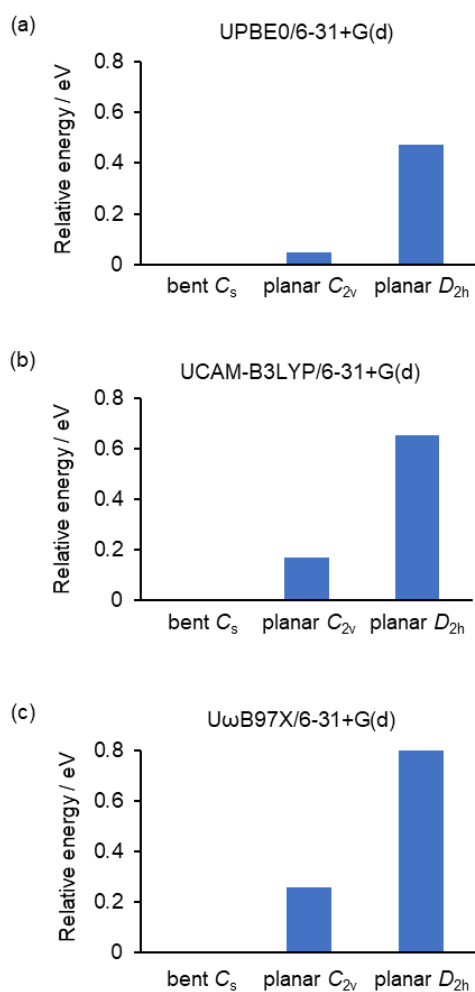
Figure S35. Comparison of the total energy of **N-FLAP'** at the T_1 optimized geometries. The energy was calculated at the optimized geometries at the level of (a) UPBE0/6-31+G(d), (b) UCAM-B3LYP/6-31+G(d), and (c) UωB97X/6-31+G(d), respectively.
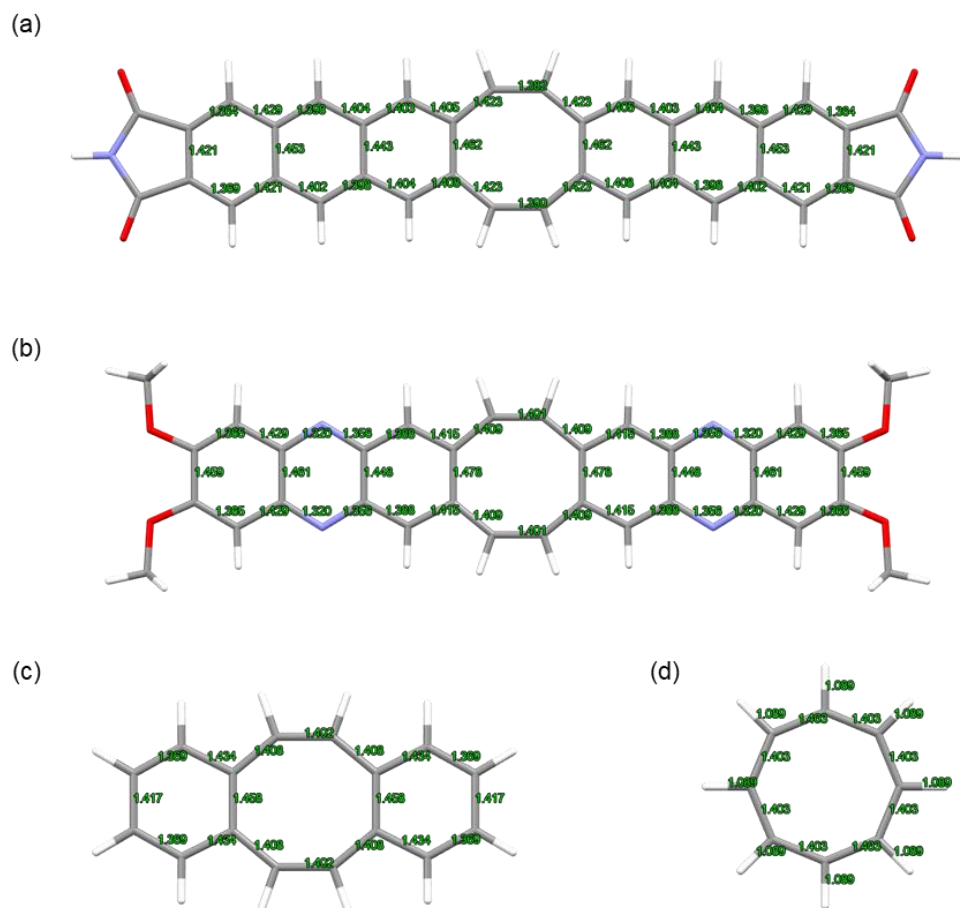
Figure S36. The S$_1$ optimized geometries and bond lengths (Å) of (a) **FLAP′** at the local minimum with planar C_{2v} symmetry, (b) **N-FLAP′** at the local minimum with planar D_{2h} symmetry, (c) DBCOT with planar D_{2h} symmetry, and (d) COT with planar D_{8h} symmetry at the TD-PBE0/6-31+G(d) level of theory.

(a)

$\theta = 0°$

(b)

(c)
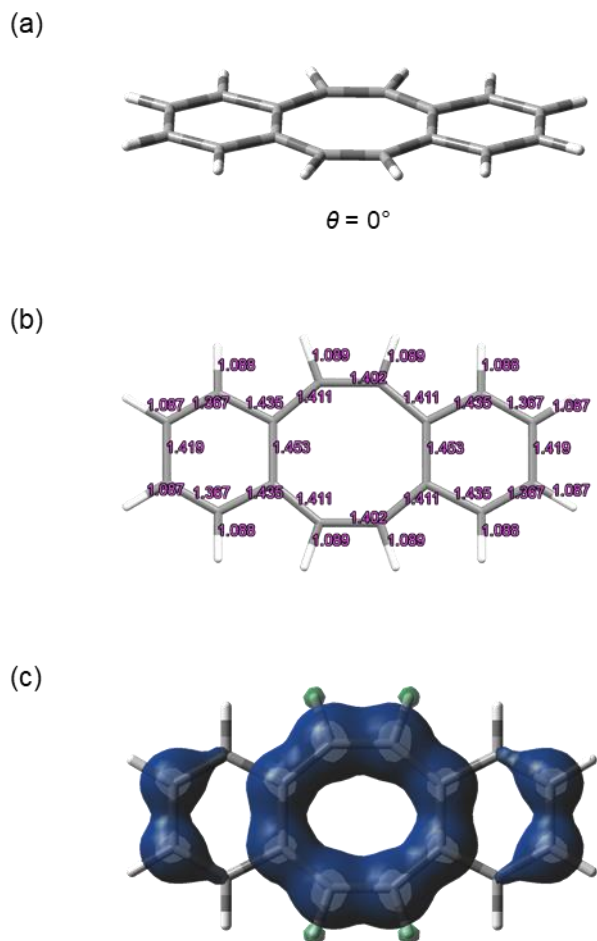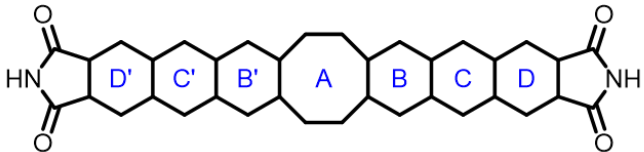
Figure S37. (a) The optimized geometry of DBCOT at the local minimum in T_1 with D_{2h} symmetry at the UPBE0/6-31+G(d) level of theory. (b) Bond length (Å) of DBCOT. (c) Spin-density-distribution plot of DBCOT in T_1 (isovalue: 0.0015).

(a)

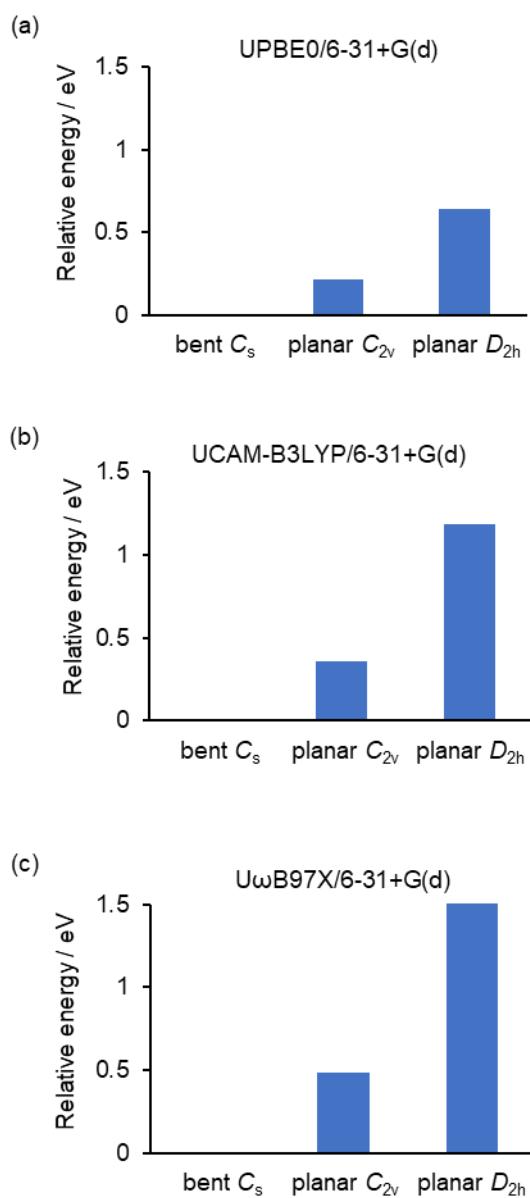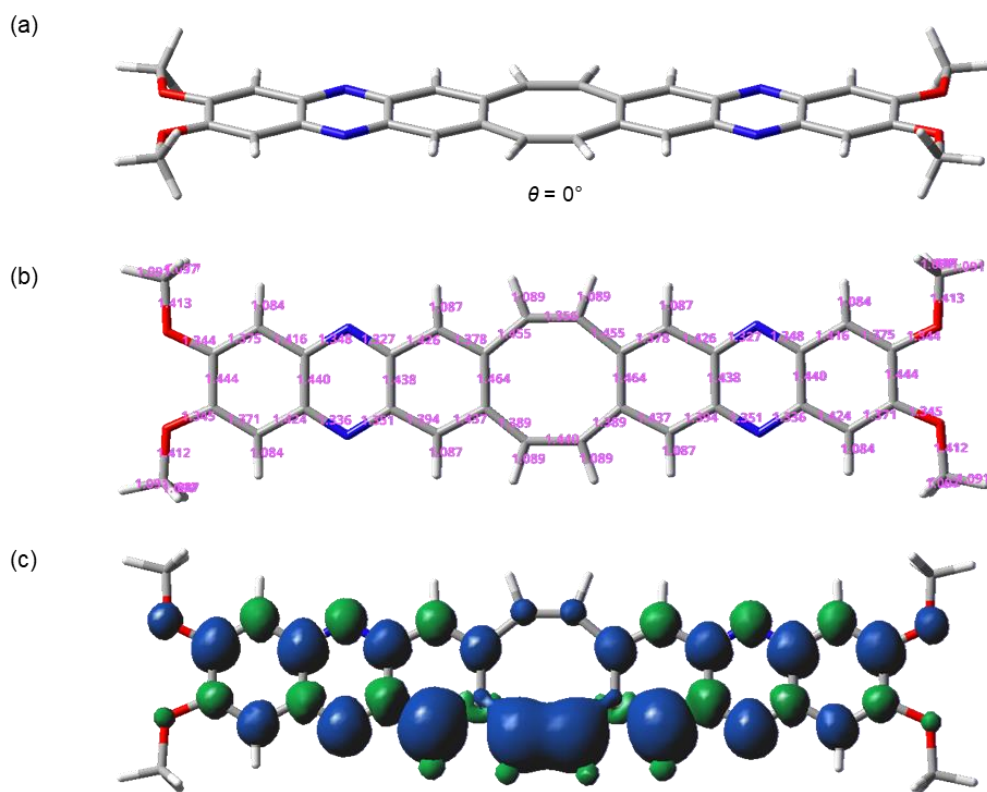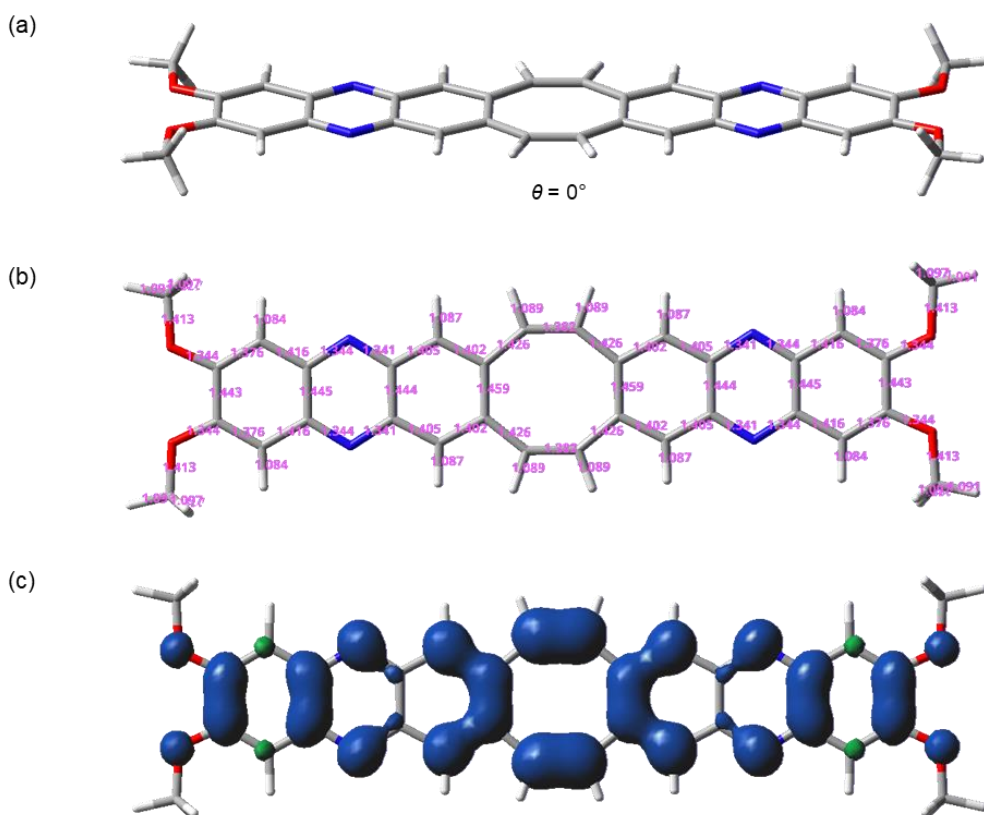
$\theta = 0°$

(b)

(c)
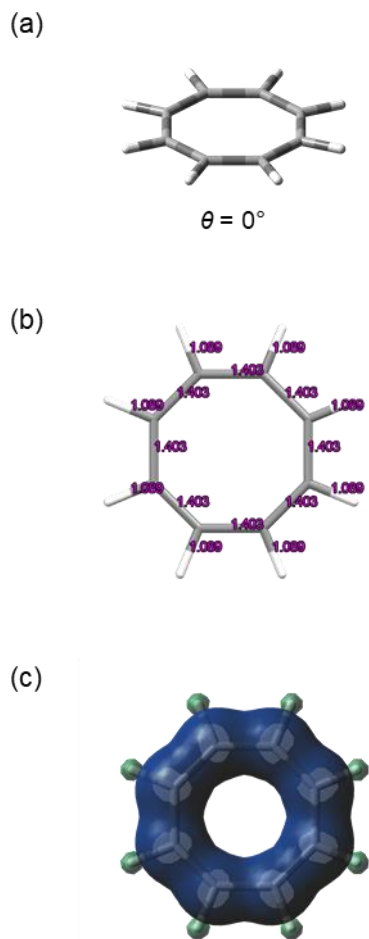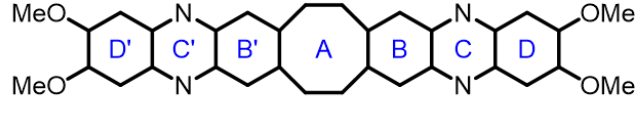
Figure S38. (a) The optimized geometry of COT at the local minimum in T_1 with D_{8h} symmetry at the UPBE0/6-31+G(d) level of theory. (b) Bond length (Å) of COT. (c) Spin-density-distribution plot of COT in T_1 (isovalue: 0.0015).

(a)
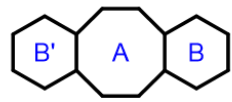
ring	A	B	C	D
NICS(0)	+2.74	−0.09	−4.18	−5.57
NICS(1)	+0.90	−3.31	−7.01	−7.60
NICS(1)$_{zz}$	+6.32	−4.00	−15.48	−17.33

(b)
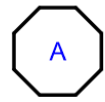
ring	A	B	C	D
NICS(0)	+2.35	−1.01	−2.67	−6.83
NICS(1)	+0.55	−4.23	−7.21	−7.75
NICS(1)$_{zz}$	+4.89	−7.28	−16.04	−16.89

(c)

ring	A	B
NICS(0)	−12.52	−8.05
NICS(1)	−12.01	−9.99
NICS(1)$_{zz}$	−33.54	−26.34

(d)

ring	A
NICS(0)	−11.11
NICS(1)	−10.90
NICS(1)$_{zz}$	−32.20

Figure S39. NICS(0), NICS(1) and NICS(1)$_{zz}$ values were calculated at the center of benzene, pyrazine, and COT rings of (a) **FLAP′**, (b) **N-FLAP′**, (c) DBCOT, and (d) COT at the local minimum in T_1 with planar C_{2v}, D_{2h}, or D_{8h} symmetry, at the UPBE0/6-31+G(d) level of theory.

(a)

ring		A	B	C	D	perimeter
HOMA	S_1	0.49	0.59	0.66	0.61	0.86
	T_1	0.25	0.47	0.69	0.69	0.75
HOMHED	S_1	0.84	0.87	0.94	0.93	0.95
	T_1	0.76	0.83	0.90	0.90	0.92

(b)

ring		A	B	C	D	perimeter
HOMA	S_1	0.41	0.43	0.59	0.36	0.80
	T_1	0.22	0.48	0.77	0.64	0.74
HOMHED	S_1	0.81	0.87	0.94	0.93	0.95
	T_1	0.76	0.83	0.92	0.89	0.92

(c)
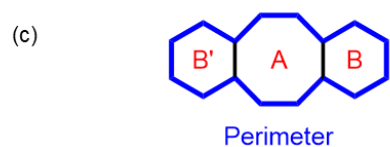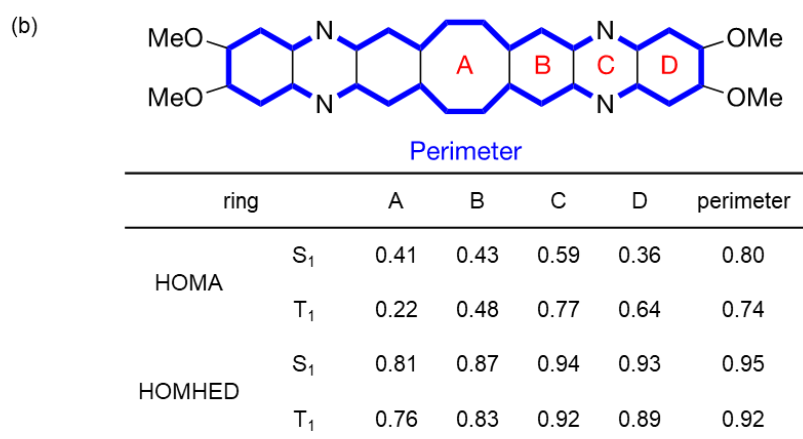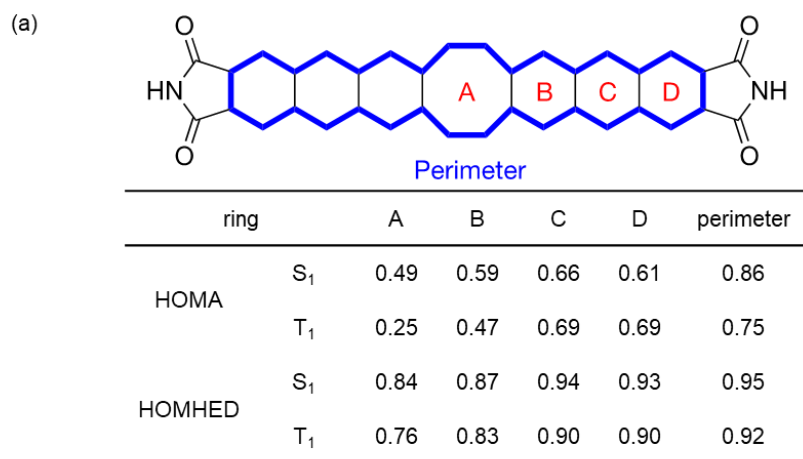
ring		A	B	perimeter
HOMA	S_1	0.62	0.54	0.78
	T_1	0.65	0.56	0.76
HOMHED	S_1	0.90	0.86	0.93
	T_1	0.91	0.86	0.92

(d)
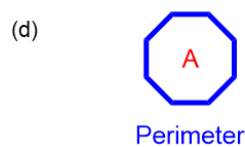
ring		A (perimeter)
HOMA	S_1	0.94
	T_1	0.94
HOMHED	S_1	0.98
	T_1	0.98

Figure S40. HOMA and HOMHED values were calculated for benzene, pyrazine, and COT ring structures and perimeters of (a) **FLAP′**, (b) **N-FLAP′**, (c) DBCOT, and (d) COT at the local minimum in S_1 and the local minimum T_1 with planar C_{2v}, D_{2h}, or D_{8h} symmetry at the TD-PBE0/6-31+G(d) and UPBE0/6-31+G(d) level of theory, respectively.

(a)

ring		A	B	C	D	B+C+D (Anthracene)	perimeter
FLU	S_1	0.015	0.016	0.015	0.015	0.009	0.007
	T_1	0.027	0.022	0.014	0.013	0.012	0.012

(b)

ring		A	B	C	D	B+C+D (Phenazine)	perimeter
FLU	S_1	0.016	0.023	0.026	0.036	0.017	0.013
	T_1	0.027	0.028	0.018	0.026	0.016	0.015

(c)

ring		A	B	perimeter
FLU	S_1	0.012	0.016	0.009
	T_1	0.011	0.016	0.009

(d)

ring		A (perimeter)
FLU	S_1	0.000
	T_1	0.001
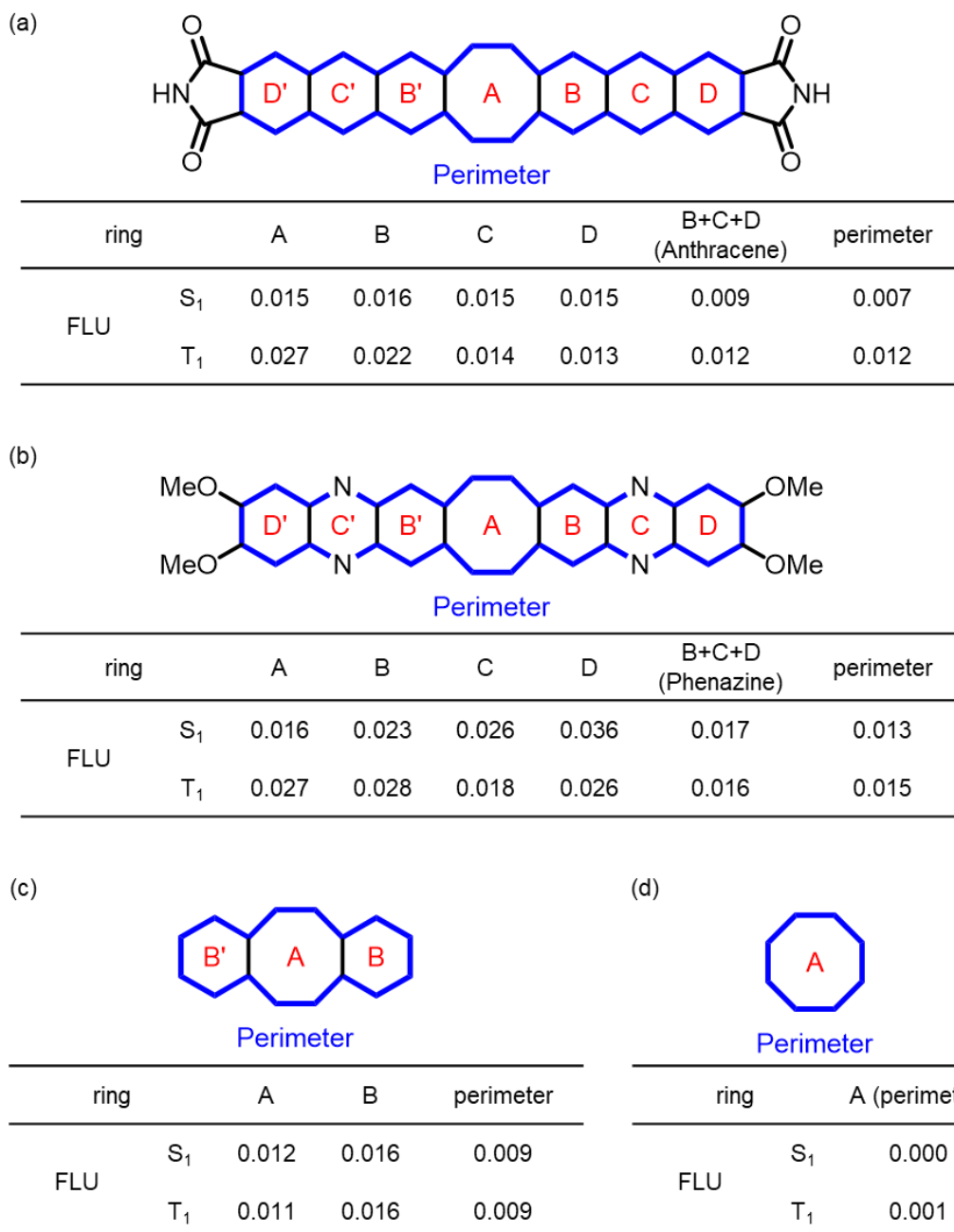
Figure S41. FLU values were calculated for benzene, pyrazine, and COT ring structures and anthracene, phenazine, and perimeters of (a) **FLAP′**, (b) **N-FLAP′** at the local minimum in S_1 and the local minimum T_1 with planar C_{2v} symmetry at the TD-PBE0/6-31+G(d) and UPBE0/6-31+G(d) level of theory, respectively. The FLU values were compared with those of (c) DBCOT and (d) COT at the local minimum in S_1 and T_1 with planar D_{2h} or D_{8h} symmetry at the TD-PBE0/6-31+G(d) and UPBE0/6-31+G(d) level of theory, respectively.

(a)

ring		B	C	D
MCI	S_1	0.0141	0.0181	0.0230
	T_1	0.0120	0.0199	0.0272

(b)

ring		B	C	D
MCI	S_1	0.0122	0.0137	0.0118
	T_1	0.0116	0.0173	0.0184

(c)

ring		B
MCI	S_1	0.0249
	T_1	0.0267
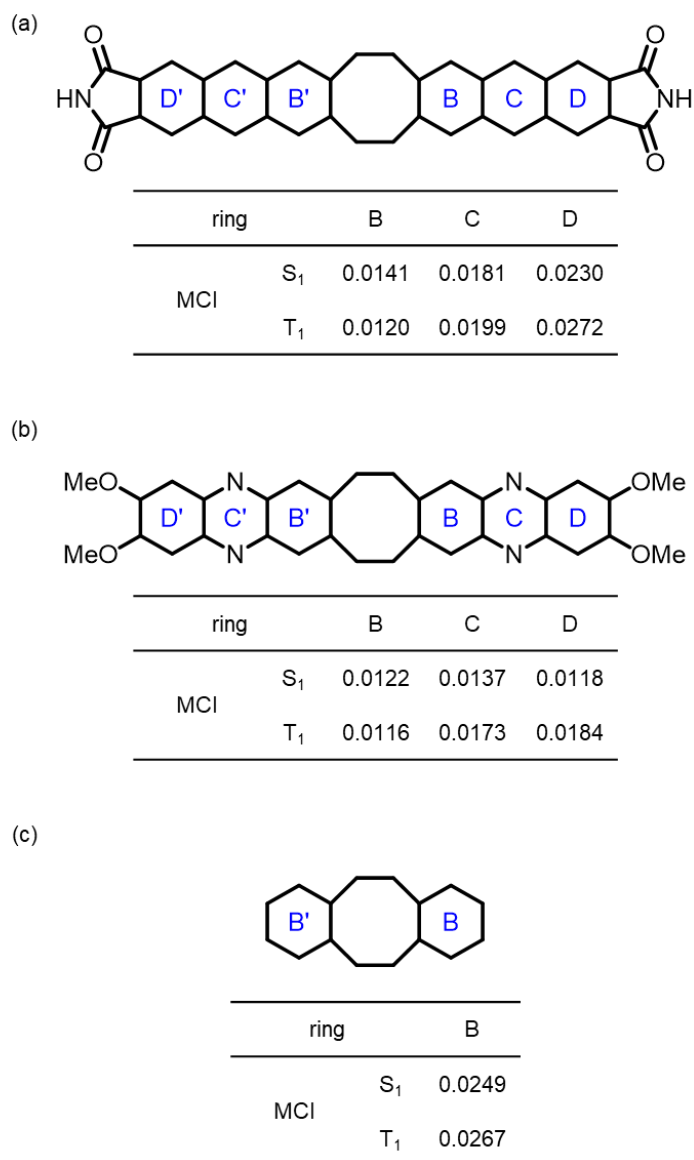
Figure S42. MCI values were calculated for benzene, pyrazine ring structures of (a) **FLAP′**, (b) **N-FLAP′** at the local minimum in S_1 and the local minimum T_1 with planar C_{2v} symmetry at the TD-PBE0/6-31+G(d) and UPBE0/6-31+G(d) level of theory, respectively. The MCI values were compared with those of (c) DBCOT at the local minimum in S_1 and T_1 with planar D_{2h} symmetry at the TD-PBE0/6-31+G(d) and UPBE0/6-31+G(d) level of theory, respectively.

Note: The value of MCI from six-membered rings (benzene/pyrazine) and the COT ring are not comparable, because MCI is a ring-size dependent measure. A ring-size independent version of MCI is constructed simply as MCI^$(1/n)$,[13] where n is the number of member rings (6 or 8). Here we do not normalize the indices, because small MCI differences are very significant in the normalized MCI.

Excitation energies and oscillator strengths at the S_0 geometries of FLAP and N-FLAP

Excited State	λ $_{nm}$, calc.	f	ΔE, eV
S1	435.33	0	2.8480
S2	418.69	0.0526	2.9613
S3	402.20	0.5538	3.0826
S4	385.84	0.0201	3.2133
S5	383.97	0.0872	3.2290
S6	372.89	0	3.3250
S7	357.15	2.1679	3.4715
S8	347.22	0.0187	3.5708
S9	332.17	0.1547	3.7326
S10	325.24	0.4249	3.8120

Table S1: Excitation energies and oscillator strengths of FLAP. TD-PBE0/6-31G(d) calculation was performed at the S_0 geometry optimized at the PBE0/6-31G(d) level.

Excited State	λ_{nm}, calc.	f	ΔE, eV
S1	413.04	0.0001	3.0018
S2	399.85	1.0869	3.1008
S3	399.05	0.0228	3.1070
S4	374.03	0.1387	3.3148
S5	371.36	0.0023	3.3386
S6	370.19	0.1076	3.3492
S7	368.55	0.0019	3.3641
S8	357.56	0	3.4675
S9	345.68	0.0857	3.5867
S10	334.28	0.1079	3.7090

Table S2: Excitation energies and oscillator strengths of N-FLAP. TD-PBE0/6-31G(d) calculation was performed at the S_0 geometry optimized at the PBE0/6-31G(d) level.

References

1. R. Kotani, H. Sotome, H. Okajima, S. Yokoyama, Y. Nakaike, A. Kashiwagi, C. Mori, Y. Nakada, S. Yamaguchi, A. Osuka, A. Sakamoto, H. Miyasaka and S. Saito, Flapping viscosity probe that shows polarity-independent ratiometric fluorescence. *Journal of Materials Chemistry C* **2017,** *5*, 5248-5256.

2. Y. Goto, S. Omagari, R. Sato, T. Yamakado, R. Achiwa, N. Dey, K. Suga, M. Vacha, S. Saito, Dynamic Polymer Free Volume Monitored by Single-Molecule Spectroscopy of a Dual Fluorescent Flapping Dopant. *Journal of the American Chemical Society* **2021,** *143*, 14306-14313.

3. A. Kundu, J. Dasgupta, Photogeneration of Long-Lived Triplet States through Singlet Fission in Lycopene H-Aggregates. *The Journal of Physical Chemistry Letters* **2021,** *12*, 1468-1474.

4. J. J. Snellenburg, S. P. Laptenok, R. Seger, K. M. Mullen, I. H. van Stokkum, *Glotaran: A Java-based graphical user interface for the R package TIMP*. **2012**.

5. M. J. Frisch, G. W. Trucks, H. B. Schlegel, G. E. Scuseria, M. A. Robb, J. R. Cheeseman, G. Scalmani, V. Barone, G. A. Petersson, H. Nakatsuji, X. Li, M. Caricato, A. V. Marenich, J. Bloino, B. G. Janesko, R. Gomperts, B. Mennucci, H. P. Hratchian, J. V. Ortiz, A. F. Izmaylov, J. L. Sonnenberg, D. Williams-Young, F. Ding, F. Lipparini, F. Egidi, J. Goings, B. Peng, A. Petrone, T. Henderson, D. Ranasinghe, V. G. Zakrzewski, J. Gao, N. Rega, G. Zheng, W. Liang, M. Hada, M. Ehara, K. Toyota, R. Fukuda, J. Hasegawa, M. Ishida, T. Nakajima, Y. Honda, O. Kitao, H. Nakai, T. Vreven, K. Throssell, J. A., Jr Montgomery, J. E. Peralta, F. Ogliaro, M. J. Bearpark, J. J. Heyd, E. N. Brothers, K. N. Kudin, V. N. Staroverov, T. A. Keith, R. Kobayashi, J. Normand, K. Raghavachari, A. P. Rendell, J. C. Burant, S. S. Iyengar, J. Tomasi, M. Cossi, J. M. Millam, M. Klene, C. Adamo, R. Cammi, J. W. Ochterski, R. L. Martin, K. Morokuma, O. Farkas, J. B. Foresman, and D. J. Fox, Gaussian 16, Revision A.03, *Gaussian*, Inc., Wallingford, **2016.** 6. (a) Schleyer, P. von R., Maerker, C., Dransfeld, A., Jiao, H., van Eikema Hommes, N. J. R. *Journal of the American Chemical Society* **1996**, *118*, 6317–6318. B) Z. Chen, C. S. Wannere, C. Corminboeuf, R. Puchta, P. v. R. Schleyer, *Chemical Reviews* **2005**, *105*, 3842−3888; c) Schleyer, P. von R., Manoharan, M., Wang, Z.-X., Kiran, B., Jiao, H., Puchta, R., and van Eikema Hommes, N.J.R. *Organic Letters*, **2001,** *3*, 2465–2468. (d) Fallah-Bagher-Shaidaei, H., Wannere, C.S., Corminboeuf, C., Puchta, R., and Schleyer, P. v. R. *Organic Letters*, **2006,** *8*, 863–866. (e) Corminboeuf, C., Heine, T., Seifert, G., Schleyer, P. von R., and Weber, J. *Physical Chemistry Chemical Physics*, **2004**, *6*, 273–276.

7. (a) T. M. Krygowski, *Journal Of Chemical Informatics and Computer Science* **1993**, *33*, 70-78; b) C. P. Frizzo, M. A. P Martins, *Structural Chemistry* **2012**, *23*, 375–380; c) T. M. Krygowski, M. K. Cyrański, *Chemical Reviews* **2001**, *101*, 1385−1419; d) T. M. Krygowski, H. Szatylowicz, O. A. Stasyuk, J. Dominikowska, M. Palusiak, *Chemical Reviews* **2014**, *114*, 6383−6422.

8.   (a) R. Herges, D. Geuenich, *Journal of Physical Chemistry A* **2001**, *105*, 3214–3220; (b) D. Geuenich, K. Hess, F. Köhler, R. Herges, *Chemical Reviews* **2005**, *105*, 3758−3772. We thank Dr. Rainer Herges and Fynn Röhricht in Christian- Albrechts-Universität zu Kiel, and Dr. Soji Shimizu in Kyushu University for their help in setting up the ACID calculation program.

9.   E. Matito, M. Duran, M. Solà, *Journal of Chemical Physics* **2005**, *122*, 14109.

10.   P. Bultinck, R. Ponec, S. Van Damme, *Journal of Physical Organic Chemistry* **2005**, *18*, 706–718.

11.   T. A. Keith, *AIMAll (Version 19.10.12)*, TK Gristmill Software, Overland Park KS, USA, **2019**. (aim.tkgristmill.com)

12.   E. Matito, *ESI-3D: Electron Sharing Indexes Program for 3D Molecular Space Partitioning*, Institute of Computational Chemistry, Girona, 2006,

13.   E. Matito, *Physical Chemistry Chemical Physics* **2016**, *18*, 11839–11846.